SANDIA REPORT

SAND2015-8012
Unlimited Release
Printed September 2015

Development of a Multi-Point Microwave Interferometry (MPMI) Method

Paul E. Specht, Marcia A. Cooper, Brook A. Jilek

Prepared by
Sandia National Laboratories
Albuquerque, New Mexico 87185 and Livermore, California 94550

Sandia National Laboratories is a multi-program laboratory managed and operated by Sandia Corporation, a wholly owned subsidiary of Lockheed Martin Corporation, for the U.S. Department of Energy's National Nuclear Security Administration under contract DE-AC04-94AL85000.

Sandia National Laboratories

Issued by Sandia National Laboratories, operated for the United States Department of Energy by Sandia Corporation.

Printed in the United States of America. This report has been reproduced directly from the best available copy.

Available to DOE and DOE contractors from
U.S. Department of Energy
Office of Scientific and Technical Information
P.O. Box 62
Oak Ridge, TN 37831

Telephone:	(865) 576-8401
Facsimile:	(865) 576-5728
E-Mail:	reports@adonis.osti.gov
Online ordering:	http://www.osti.gov/bridge

Available to the public from
U.S. Department of Commerce
National Technical Information Service
5285 Port Royal Rd
Springfield, VA 22161

Telephone:	(800) 553-6847
Facsimile:	(703) 605-6900
E-Mail:	orders@ntis.fedworld.gov
Online ordering:	http://www.ntis.gov/help/ordermethods.asp?loc=7-4-0#online

SAND2015-8012
Unlimited Release
Printed September 2015

Development of a Multi-Point Microwave Interferometry (MPMI) Method

Paul E. Specht, Marcia A. Cooper, and Brook A. Jilek
Sandia National Laboratories
P.O. Box 5800
Albuquerque, NM 87185

Abstract

A multi-point microwave interferometer (MPMI) concept was developed for non-invasively tracking a shock, reaction, or detonation front in energetic media. Initially, a single-point, heterodyne microwave interferometry capability was established. The design, construction, and verification of the single-point interferometer provided a knowledge base for the creation of the MPMI concept. The MPMI concept uses an electro-optic (EO) crystal to impart a time-varying phase lag onto a laser at the microwave frequency. Polarization optics converts this phase lag into an amplitude modulation, which is analyzed in a heterodyne interferometer to detect Doppler shifts in the microwave frequency. A version of the MPMI was constructed to experimentally measure the frequency of a microwave source through the EO modulation of a laser. The successful extraction of the microwave frequency proved the underlying physical concept of the MPMI design, and highlighted the challenges associated with the longer microwave wavelength. The frequency measurements made with the current equipment contained too much uncertainty for an accurate velocity measurement. Potential alterations to the current construction are presented to improve the quality of the measured signal and enable multiple accurate velocity measurements.

Acknowledgments

Funding for this project was provided through the Early Career Laboratory Directed Research and Development (EC LDRD) program. Thanks is due to the management team of Leanna Minier (Org. 2554), John Benage Jr. (Org. 1646), and Gordon Leifeste (Org. 1647) for helping to coordinate the work. Wayne Trott, Adam Sapp, Mike Oliver, Mike Kaneshige, and Ben Hanks assisted in the development of the single-point microwave interferometer. Daniel Dolan provided invaluable insight about heterodyne interferometry methods and Fourier transform analysis. In addition, Dan along with Tommy Ao and Sean Grant loaned lasers and several optical components for the project. Thanks go to the entire Dynamic Integrated Compression Experimental (DICE) facility team (Randy Hickman, Keith Hodge, Nicole Cofer, and Joshua Usher) for providing a workspace for the project. The project is also indebted to Sheri Payne and Richard Hacking of National Security Technologies (NSTec) for providing advice and several optical components. Lastly, thanks goes to Nick Miller for helping to keep the project on budget.

Contents

Appendix

List of Figures

List of Tables

Chapter 1

Motivation and Introduction

A multi-point microwave interferometer (MPMI) concept was developed to non-invasively monitor the internal transit of a shock, detonation, or reaction front in energetic media. Standard optical interferometry techniques, such as VISAR (Velocity Interferometer System for Any Reflector) [3] and PDV (Photonic Doppler Velocimetry) [44] provide only a single-point measurement of a surface or interface velocity. While there does exist a spatially-resolved optical method, ORVIS (Optically Recording Velocity Interferometer System) [6], it suffers from the same limitation of providing only surface or interface measurements. Without a direct, internal measurement, it is necessary to infer the material's state. Alternate diagnostics embedded in the sample, such as electromagnetic gauges, inherently disrupt the state of the shock or reaction front measured. The only method to obtain a non-invasive internal velocity measurement in energetic media is with microwave interferometry. Most energetic media is transparent in the microwave regime, but the dielectric discontinuity at a shock, detonation, or reaction front generates a back reflection, enabling an interferometric measurement [4]. Current microwave interferometers also only provide a continuum measurement, averaging out the spatial characteristics. These factors limit the effectiveness of these diagnostics in understanding the complex wave and material interactions affecting the thermal, mechanical, and chemical response of heterogeneous energetic materials. Coupling laser and microwave interferometry techniques with terahertz spectroscopic methods, a MPMI concept was develop to bridge this experimental gap and provide an internal, spatially-resolved interferometric measurement.

The report begins with a brief description of current, state-of-the-art microwave interferometers. It then discusses the design, construction, and verification of a single-point microwave interferometer, reestablishing the capability at Sandia. Building on this work, the MPMI concept is presented. A version of the MPMI concept was constructed for validating the extraction of the microwave frequency through the EO modulation of a laser beam. The limitations and technical challenges raised by these initial tests are discussed. Suggested alterations to the design are then proposed for making an accurate velocity measurement with the MPMI concept.

This page intentionally left blank.

Chapter 2

The Single-Point Microwave Interferometer

Microwave interferometers utilize a heterodyne design to provide a single, continuum measurement of the velocity of a dielectric discontinuity. This section begins with a brief discussion of microwave interferometer design. More detailed descriptions are available in the literature [7, 8, 15, 16, 21, 24, 26, 31, 40, 43, 42, 41, 47]. The construction and verification of a 35.2 GHz single-point microwave interferometer is then presented.

2.1 Single-Point Microwave Interferometer Design

A simple, heterodyne microwave interferometer design is shown schematically in Figure 2.1. The microwave source is divided into two legs by a microwave coupler. The diverted signal is used as a reference. The transmitted signal is directed towards a circulator. The microwaves entering port 1 exit port 2 and are directed to the experimental surface. The reflected signal returns to port 2 on the circulator and exits at port 3. The reference and reflected signals are compared by a mixer. Mathematically, this is expressed with their combined electric fields.

$$E(t) = A_1 \cos(2\pi f_0 t + \phi_1) + A_2 \cos(2\pi f(t) t + \phi_2) \tag{2.1}$$

Here, f_0 is the initial frequency of the source, $f(t)$ is the reflected, Doppler shifted frequency, and ϕ_1 and ϕ_2 are the phases of each wave. The parameters A_1 and A_2 represent the intensities of the reference and reflected signals, respectively. The reflected, Doppler shifted frequency is related to the experimental surface velocity, $v(t)$ [12].

$$f(t) = f_0 \frac{c + v(t)}{c - v(t)} \approx f_0 \left(1 + \frac{2v(t)}{c}\right) \tag{2.2}$$

The speed of light in the material, c, depends on the material's relative permittivity, ϵ_r.

$$c = \frac{c_0}{\sqrt{\epsilon_r}} \tag{2.3}$$

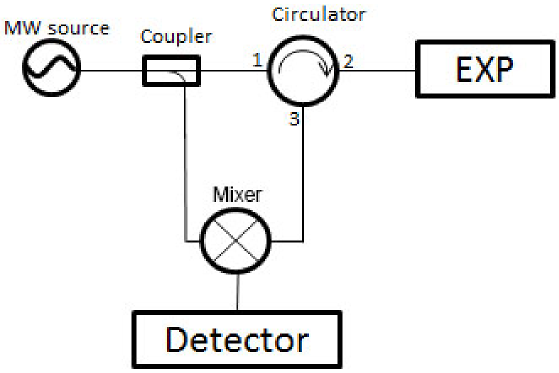

Figure 2.1: Block diagram of a simple, heterodyne microwave interferometer.

The output of the mixer is sent to a detector. The detector records the intensity, which is the square of the electric field. Since the mixer acts as a low pass filter, only the difference between the two frequencies is recorded.

$$I(t) = E(t)^2 = \cos\left(2\pi\left(f(t) - f_0\right)t + \Phi\right) \tag{2.4}$$

Any delay between the reflected and reference legs is accounted for in the relative phase lag, $\Phi = \phi_2 - \phi_1$. The frequency of the recorded signal represents a beat frequency between the reference and reflected signals and relates to the velocity.

$$f_b(t) = f(t) - f_0 = f_0 \frac{2v(t)}{c} \tag{2.5}$$

At a constant velocity, a 2π phase shift occurs for every have wavelength of motion, $\frac{\lambda_0}{2}$.

$$\Delta x = \frac{v(t)}{f_b(t)} = \frac{c}{2f_0} = \frac{\lambda_0}{2} \tag{2.6}$$

Counting the maxima and minima in the signal gives the displacement of the measurement surface every quarter wavelength. Alternately, a fast Fourier transform (FFT) can extract the beat frequency and directly relate it to the velocity through Equation 2.5. Since the wavelengths of microwaves are on the order of millimeters, this design gives rather poor resolution of the front displacement.

To increase the displacement resolution, most current microwave interferometers utilize a quadrature design [7, 16, 24, 26, 40, 43, 42, 41]. This is shown schematically in Figure 2.2. In this configuration, the reference and reflected signals are combined in an IQ mixer. In the IQ mixer, both the reference and reflected signals are split by a coupler. One of the reference signals is phase lagged 90^0 by a phase shifter. One reflected signal is combined with the original reference signal, labeled the in-phase (I) channel. The other reflected signal is combined with the phase lagged reference, labeled the quadrature (Q) channel. The

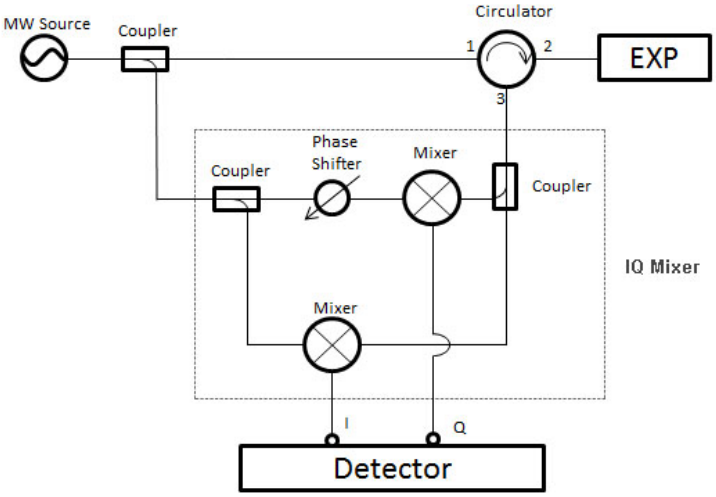

Figure 2.2: Block diagram of a quadrature-based microwave interferometer.

phase difference between the two signals, $\Theta(t)$, is directly related to the displacement of the measured surface [12, 4].

$$\tan(\Theta(t)) = \tan(\epsilon) + \frac{Q(t)}{I(t)}R(t)\sec(\epsilon) \tag{2.7}$$

$$\Delta x = \frac{\lambda_0}{4\pi}\Theta(t) \tag{2.8}$$

Here, ϵ is the phase error between the I and Q channels (*i.e.* the deviation from 90^o), $Q(t)$ and $I(t)$ are the in-phase and quadrature signals, and $R(t)$ is the amplitude ratio between the two signals. IQ mixers have phase resolutions on the order of 5^o to 10^o, which provides resolutions around 1% of the wavelength [4]. It is possible to employ frequency downshifting to achieve better phase resolution [15, 31, 47, 41].

2.2 Single-Point Microwave Interferometer Construction

A 35.2 GHz, quadrature-based microwave interferometer was constructed at Sandia. A schematic of its design is presented in Figure 2.3. The source (Millitech PLS-28-A-002) consists of a 17.6 GHz Gunn diode output into an active multiplier chain to double its frequency. It is capable of producing slightly over 23 dBm. The source can accept an external 10 MHz signal, allowing it to be synchronized, or phase locked, with another source. A phase lockable source enables frequency downshifting in the future to improve the spatial resolution [42, 41]. The output of the microwave source is split with a 10 dB coupler (Millitech CL3-28-S1000). The weaker signal split off of by the coupler is used as the reference. The stronger

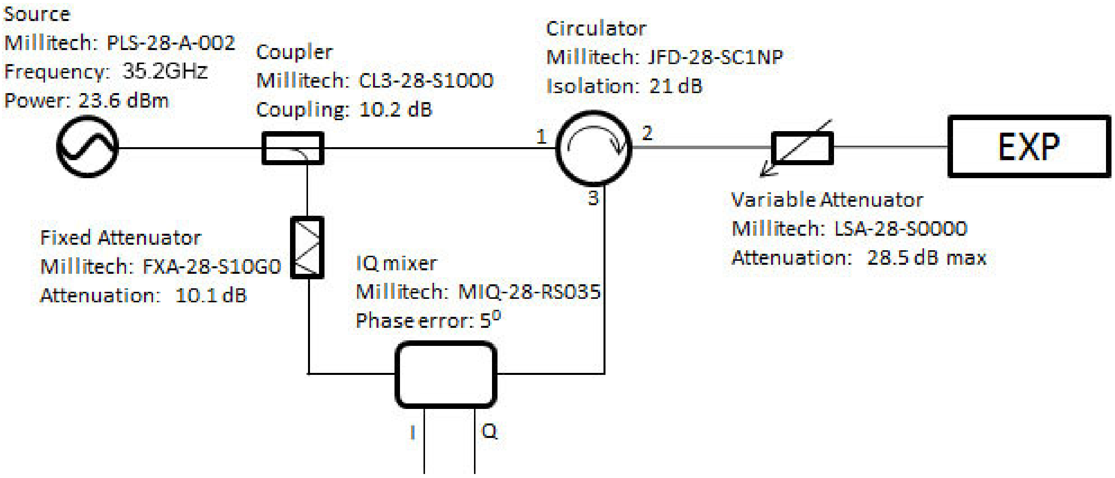

Figure 2.3: Block diagram of the Sandia single-point microwave interferometer.

transmitted signal is sent to a circulator (Millitech JFD-28-SC1NP), which directs it toward the measurement surface. A variable attenuator (LSA-28-S0000), capable of around 30 dB of attenuation, is placed after the circulator to adjust the power imparted to the measurement surface. The microwave energy reflected from the measurement surface enters the circulator and is directed toward an IQ mixer (Millitech MIQ-28-RS035). The IQ mixer compares the reflected signal with the reference signal, which passes through a 10 dB fixed attenuator. This ensures the reference is within the power requirements of the IQ mixer. The IQ mixer in this interferometer has a phase error of 5^o and is 100^o out of phase. All lines in the schematic represent rectangular WR-28 waveguides.

The interferometer is housed in a steel electrical enclosure. Power is provided to the interferometer by a standard power cable plugged into a 110 VAC outlet. A commercial AC/DC converter generates 15VDC to run all the components. The 15VDC used is above the power requirements for many of the components. However, all the components have internal voltage regulators. Running higher voltage into the components does not damage them, it just increase the heat dissipated [27]. A computer fan was incorporated into the steel enclosure to help cool the components. The interferometer was run for several days with no noticeable degradation in performance. A photograph of the interferometer is presented in Figure 2.4

2.3 Single-Point Microwave Interferometer Verification

To ensure the constructed 35.2 GHz interferometer was operating properly, it was used to measure the motion of a silvered mirror (Thorlabs PF40-03-P01). A translation stage (Thorlabs MTS50-Z8) was used to move the silvered mirror at a prescribed velocity. Five

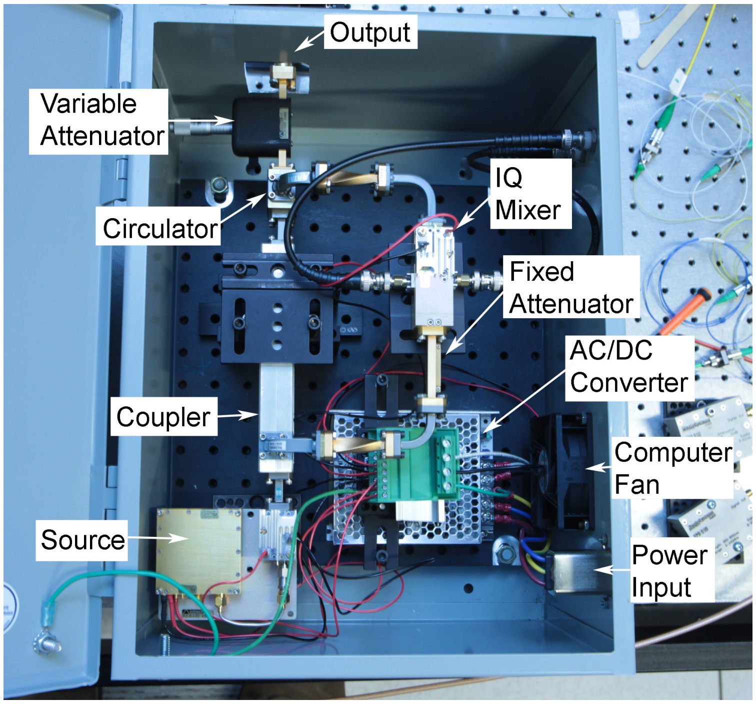

Figure 2.4: Photograph of the Sandia single-point microwave interferometer.

measurements were taken with the translation stage moving at 1 mm/s, and 3 measurements were taken with the translation stage moving at 2 mm/s. The translation stage was measured to have a velocity error of 0.02 mm/s at 1 mm/s and 0.05 mm/s at 2 mm/s. Figure 2.5 shows representative I and Q signals recorded with the interferometer. The recorded I and Q channels have very different amplitudes. The IQ mixer was designed to provide as close to a 90^o phase lag as possible and not for equal output amplitudes.

The verification tests were analyzed using a MATLAB® analysis program capable of peak counting, quadrature analysis, and a simple FFT method. A description of the MATLAB® analysis program is presented in Appendix A. The results of all eight verification experiments are summarized in Table 2.1. The results show the velocity found using peak counting on the I and Q channels along with quadrature analysis. The results are highly reproducible and match well with the prescribed velocity. No errors are reported but are under 0.02 mm/s for both methods. Figure 2.6 show the results obtained using peak counting on the I channel along with quadrature analysis for Test 2. The methods match well.

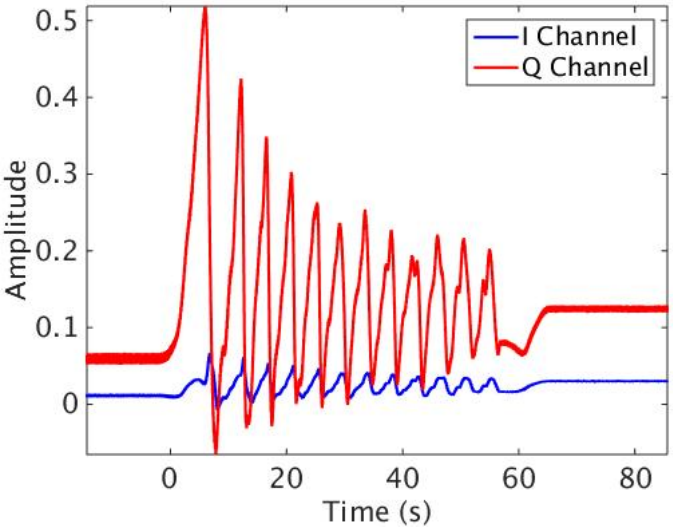

Figure 2.5: Typical I and Q signals obtained during verification testing of the 35.2 GHz microwave interferometer.

Table 2.1: Results of the verification tests on the 35.2 GHz microwave interferometer using peak counting and quadrature analysis.

Test Number	Prescribed Velocity (mm/s)	Peak Counting I (mm/s)	Peak Counting Q (mm/s)	Quadrature (mm/s)
1	1.0	0.978	0.974	0.984
2	1.0	0.978	0.974	0.984
3	1.0	0.991	0.990	0.988
4	1.0	0.990	0.990	0.993
5	1.0	0.990	0.990	0.993
6	2.0	1.988	1.979	1.976
7	2.0	1.989	1.979	1.977
8	2.0	1.989	1.979	1.980

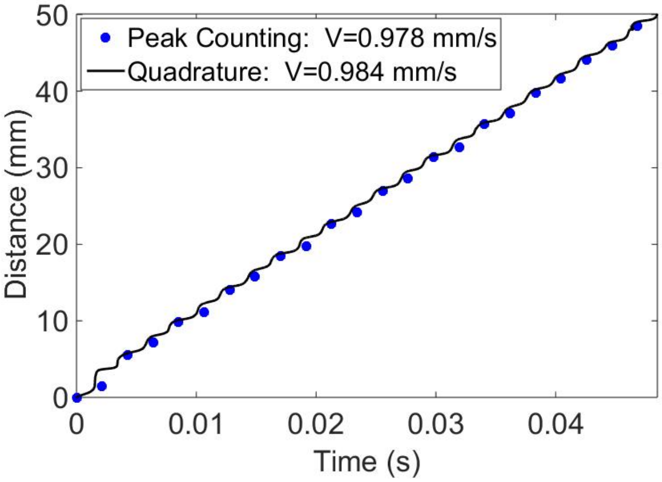

Figure 2.6: Velocity measured by the microwave interferometer using peak counting on the I channel and quadrature analysis for Test 2.

Chapter 3

Generation of the MPMI Concept

A novel interferometer configuration is needed to obtain spatial information in the microwave regime. This section outlines the process used to develop the MPMI concept through the coupling of laser and microwave interferometry techniques with terahertz spectroscopic methods.

3.1 Selection of the Interferometer Configuration

There exists a spatially-resolved, optical interferometry technique, ORVIS [6]. It is a homodyne interferometer and essentially a slight modification on a wide-angle Michelson interferometer. Microwave-based, Michelson-type interferometers were constructed in the past to measure dielectric constants [9] and the speed of light [10]. Unfortunately, complications arise when using a similar homodyne configuration to measure a surface velocity, due to the longer microwave wavelengths.

This is evident when considering the operation of a Michelson interferometer at a microwave wavelength. Such an interferometer is shown schematically in Figure 3.1. In this homodyne interferometer, a single signal is split along two paths of differing lengths before being recombined.

$$E(t) = A_1 \cos(2\pi f(t)t + \phi_1) + A_2 \cos(2\pi f(t)(t + \tau) + \phi_2) \tag{3.1}$$

$$\tau = \frac{2d}{c} \tag{3.2}$$

The parameters A_1, A_2, ϕ_1, and ϕ_2 are the intensities and phase lags of each leg. Both signals are assumed to have the same frequency $f(t)$ over their relative time delay, τ. This is the commonly used VISAR approximation [12]. The time delay is related to the difference in path lengths, d, and the speed of light in the media, c, which is determined by Equation 2.3. A detector placed at the output of the interferometer records the intensity.

$$\begin{aligned} I(t) &= E(t)^2 \\ &= A_1^2 \cos^2(2\pi f(t)t + \phi_1) + 2A_1A_2 \cos(2\pi f(t)t + \phi_1)\cos(2\pi f(t)(t + \tau) + \phi_2) \\ &\quad + A_2^2 \cos^2(2\pi f(t)(t + \tau) + \phi_2) \end{aligned} \tag{3.3}$$

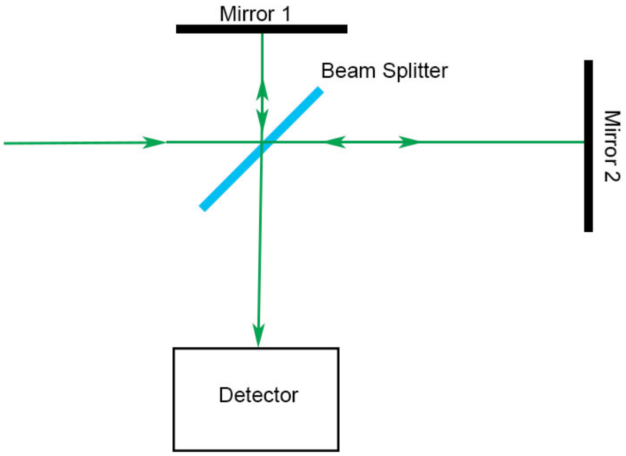

Figure 3.1: Block diagram of a Michelson interferometer.

If the frequency of the wave is significantly larger than the detector bandwidth, the recorded signal is the time average of the intensity, $\langle I(t)\rangle$ [12]. This enables simplification with the following relations.

$$\langle \cos^2(\omega)\rangle = \frac{1}{2} \tag{3.4a}$$

$$\cos(\omega_1)\cos(\omega_2) = \frac{1}{2}\cos(\omega_1+\omega_2) + \frac{1}{2}\cos(\omega_1-\omega_2) \tag{3.4b}$$

$$\langle \cos(\omega_1)\rangle = 0 \tag{3.4c}$$

$$\langle \cos(\omega_1 + \ldots + \omega_n)\rangle = 0 \tag{3.4d}$$

The recorded signal is simplified to one frequency term.

$$\langle I(t)\rangle = \frac{1}{2}\left(A_1^2 + A_2^2\right) + \cos(2\pi f(t)\tau + \phi_2 - \phi_1) \tag{3.5}$$

If the frequency of the signal entering the interferometer changes due to a Doppler shift imparted by a surface velocity, $v(t)$, the recorded intensity changes based on Equation 2.2.

$$\langle I(t)\rangle = A + \cos\left(2\pi\tau f_0\left(1 + \frac{2v(t)}{c}\right)\right) \tag{3.6}$$

The relative phase difference is ignored and the leading term is represented by a single variable, A, for simplicity. The velocity necessary to achieve a 2π phase shift, or one fringe, is determined by the original signal frequency and the interferometer configuration.

$$v_{2\pi} = \frac{c}{2f_0\tau} \tag{3.7}$$

The above expression illustrates the limitations of a homodyne interferometer in the microwave regime. A 100 GHz microwave signal requires $\tau = 1.5\mu$s to achieve a fringe every

1000 m/s. Not only does such a long delay eliminate the simplifications provided by the VISAR approximation, it leads to unreasonable delay sections. To achieve such a long delay, a 450 m path difference or an etalon with an index of refraction of 1.5 and a length of 300 m is needed.

A spatially-resolved interferometer, such as ORVIS, has an added complication. In an ORVIS, a mirror is rotated by a small angle, $\frac{\alpha}{2}$, and moved forward. This generates fringes of equal thickness, or Fizeau fringes [18]. This results from a variable delay along the laser width.

$$\tau(x) = \tau_d + \frac{x}{c}\sin(\alpha) \tag{3.8}$$

Here, τ_d is the time delay between the two legs without titling the mirror and x is the position along the beam width. The distance separating the fringes, d, is related to the mirror angle [6].

$$d = \frac{\lambda_0}{\sin(\alpha)} \tag{3.9}$$

Since α is a characteristically small angle (typically less than 0.005 rad) [6], the longer wavelength of the microwaves leads to impractical fringe spacings. A 100 GHz microwave signal has a wavelength of roughly 3 mm in air. With $\alpha = 0.005$ radians, the fringe spacing of a 100 GHz interferometer is 60 cm.

A heterodyne design is the only practical choice for a microwave interferometer. Current heterodyne microwave interferometers utilize waveguides, which destroy any spatial information. An open beam is needed to preserve the spatial information. This imposes challenges associated with collimating a microwave beam over large distances and detecting it on timescales fast enough for shock physics experimentation.

3.2 MPMI Design

To eliminate some of the technical challenges associated with an open microwave beam, a MPMI design was developed based on the electro-optic (EO), or Pockel, effect. EO crystals act as variable waveplates, due to their lack of inversion symmetry [28]. Their birefringence is dependent on the strength of an applied electric field, E [28].

$$\delta = \frac{2\pi l n^3 r_{ij}}{\lambda} E \tag{3.10}$$

Here, δ is the phase lag between the ordinary and extraordinary rays, l is the thickness of the crystal, n is the index of refraction of the crystal, λ is the wavelength of the light, and r_{ij} is the EO coefficient of the crystal.

Past researchers used this phenomena to obtain real-time imaging of RF signals [45, 46, 34, 33, 35]. This work centered on converting the phase lag generated by the EO crystal into

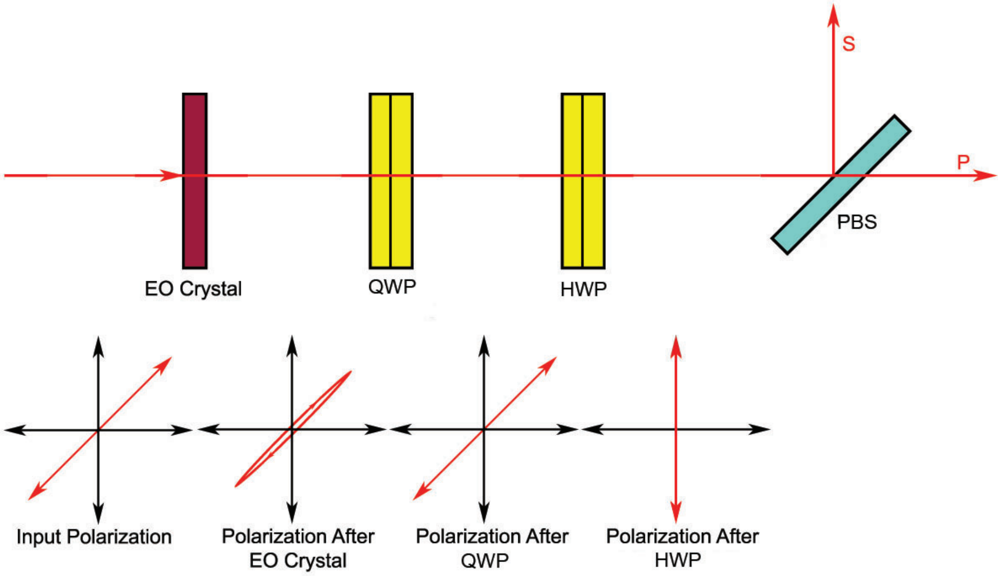

Figure 3.2: Schematic illustrating the use of an EO crystal and polarization optics to generate amplitude modulation in a laser.

an amplitude modulation with polarization optics. This is illustrated schematically in Figure 3.2. A linearly polarized laser was sent through an EO crystal subjected to a microwave signal. The electric field of the microwaves induced a phase lag in the laser, generating an elliptical polarization state. A quarter waveplate (QWP) placed after the EO crystal was oriented to return the laser to a linear polarization state. A half waveplate (HWP) was used to rotate the polarization state so it was completely transmitted by a polarizing beam splitter (PBS). If the applied electric field changes, the phase lag imparted by the EO crystal changes per Equation 3.10. If the orientations of the waveplates are constant, changes to the applied electric field generate a small reflected signal at the PBS. If the applied electric field modulates at a characteristic frequency, the amplitude of the reflected signal also modulates at that frequency. This intensity modulation allowed the past researchers to visualize a microwave signal.

The ability of this optical configuration to impart a microwave frequency onto a laser enables its use as the basis of a heterodyne interferometer. A simplified schematic of such an interferometer is presented in Figure 3.3. This design is slightly different than that previously proposed by the authors [36]. The main difference is the reflection of the laser after the EO crystal by a dielectric mirror or, preferably, by a highly reflective (HR) coating on the crystal itself. Due to time constraints, a HR coating was not applied the EO crystal used in this work. The reasons for this redesign are twofold. First, it involves fewer optical elements. Second, by reflecting of the back side of the EO crystal, the laser makes two passes through it. This effectively doubles the crystal thickness, doubling the phase lag generated.

In the MPMI concept, a microwave source, operating at frequency f_{MW}, is projected from an antenna towards the measurement surface by a beam splitter. An effective microwave beam splitter consists of two plastic sheets with quarter wavelength thickness [10]. The ratio between the power transmitted and reflected is determined by their separation [10]. The reflected microwave signal at frequency $f'_{MW}(t)$ is directed towards the EO crystal by the beam splitter. The electric field of the reflected microwave signal imparts a phase lag onto a laser operating at frequency f_1, which passes through the EO crystal and reflects off the dielectric mirror. A QWP and PBS convert this phase lag into an amplitude modulation at the reflected microwave frequency, $f'_{MW}(t)$. The inclusion of a HWP is unnecessary in this design, since a HWP imparts a π phase lag between polarization components. Passage through it twice yields the initial polarization state.

The electric field of this amplitude modulated signal is represented with the following.

$$E = A_2[1+\cos(2\pi f'_{MW}(t)t+\phi_{MW})]\cos(2\pi f_1 t+\phi_1)+A_0 = A_2[1+\cos(\beta)]\cos(\alpha)+A_0 \tag{3.11}$$

The amplitude of the polarization component transmitted by the PBS, A_2, is proportional to the imparted phase lag, δ. The term A_0 represents the amount of light transmitted by the PBS when no electric field is present. This may result from slight deviations from the ideal rotation angles of the waveplates or bleed through in the PBS. The amplitude modulated beam is combined with a second laser at frequency f_2.

$$\begin{aligned} E &= A_2[1+\cos(2\pi f'_{MW}(t)t+\phi_{MW})]\cos(2\pi f_1 t+\phi_1)+A_0+A_3\cos(2\pi f_2 t+\phi_2) \\ &= A_2[1+\cos(\beta)]\cos(\alpha)+A_0+A_3\cos(\gamma) \end{aligned} \tag{3.12}$$

The addition of the second laser after modulation by the EO crystal ensures ample light is sent to the detector, allowing detection of experimental signals several dB lower than the reference [19]. The detector records the intensity of the combined lasers.

$$\begin{aligned} I = E^2 = &A_2^2\cos(\alpha)^2+2A_2^2\cos(\alpha)^2\cos(\beta)+2A_0A_2\cos(\alpha)+2A_2A_3\cos(\alpha)\cos(\gamma)+ \\ &A_2^2\cos(\alpha)^2\cos(\beta)^2+2A_0A_2\cos(\alpha)\cos(\beta)+2A_2A_3\cos(\alpha)\cos(\beta)\cos(\gamma)+ \\ &A_0^2+2A_0A_3\cos(\gamma)+A_3^2\cos(\gamma)^2 \end{aligned} \tag{3.13}$$

The intensity is expanded with Equations 3.4a and 3.4b.

$$\begin{aligned} I = &A_2^2\cos(\alpha)^2+\frac{1}{2}A_2^2\cos(2\alpha+\beta)+\frac{1}{2}A_2^2\cos(2\alpha-\beta)+A_2^2\cos(\beta)+2A_0A_2\cos(\alpha)+ \\ &A_2A_3\cos(\alpha+\gamma)+A_2A_3\cos(\alpha-\gamma)+\frac{1}{4}A_2^2+\frac{1}{4}A_2^2\cos(2\alpha)+\frac{1}{4}A_2^2\cos(2\beta)+ \\ &\frac{1}{8}A_2^2\cos(2\alpha+2\beta)+\frac{1}{8}A_2^2\cos(2\alpha-2\beta)+A_0A_2\cos(\alpha+\beta)+A_0A_2\cos(\alpha-\beta)+ \\ &\frac{1}{2}A_2A_3\cos(\alpha+\beta+\gamma)+\frac{1}{2}A_2A_3\cos(\alpha+\beta-\gamma)+\frac{1}{2}A_2A_3\cos(\alpha-\beta+\gamma)+ \\ &\frac{1}{2}A_2A_3\cos(\alpha-\beta-\gamma)+A_0^2+2A_0A_3\cos(\gamma)+A_3^2\cos(\gamma)^2 \end{aligned} \tag{3.14}$$

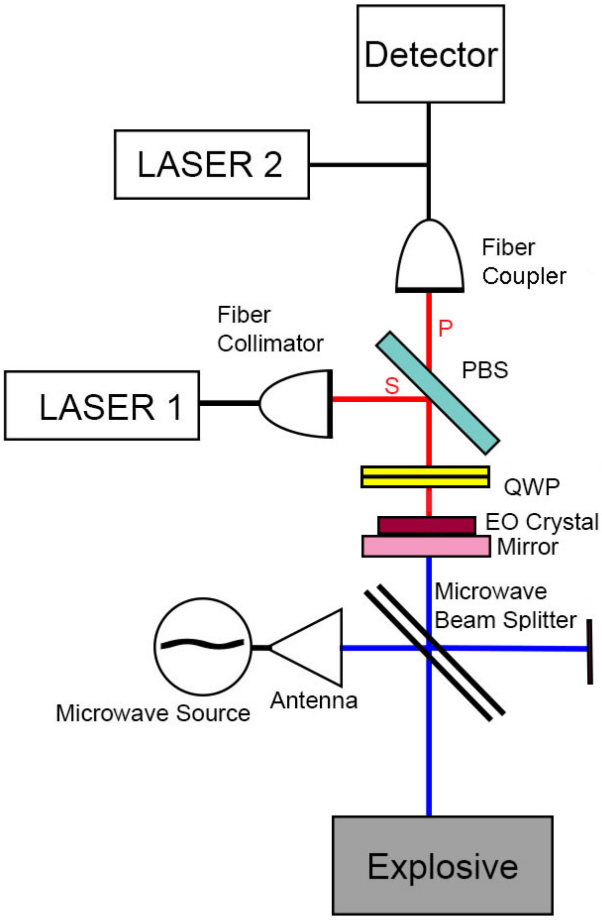

Figure 3.3: Schematic illustrating the MPMI concept.

There are numerous frequency terms in the intensity, but careful selection of the detector bandwidth provides a means to measure the microwave frequency.

The laser frequencies are on the order of 10^{14} Hz, while the microwave frequency is 10s of GHz. If these frequencies are above the detector's bandwidth, only their time average is measured. Any terms involving only these frequencies or their summations are zero. In addition, the laser frequencies are large compared to the microwave frequency. Terms involving the difference between a laser frequency and the microwave frequency are outside the detectors range and not recorded. Equation 3.14 then simplifies to the following.

$$\begin{aligned}\langle I\rangle =&\frac{3}{4}A_2^2 + A_2A_3\cos(\alpha-\gamma) + \frac{1}{2}A_2A_3\cos(\alpha+\beta-\gamma)+\\ &\frac{1}{2}A_2A_3\cos(\alpha-\beta-\gamma) + A_0^2 + \frac{1}{2}A_3^2\end{aligned} \tag{3.15}$$

If the laser frequencies are constant in time, but not equal, they generate a constant beat frequency.

$$f_b = |f_2 - f_1| = |\gamma - \alpha| \tag{3.16}$$

Suppose the beat frequency is slightly above or below the microwave signal, such that the difference is within the detector bandwidth, f_d.

$$|f_b - f'_{MW}(t)| < f_d \tag{3.17}$$

If both f_b and f_{MW} are above f_d the only recordable signals are the DC component and $|f_b - f'_{MW}(t)|$.

$$\begin{aligned}\langle I\rangle =&A_0^2 + \frac{3}{4}A_2^2 + \frac{1}{2}A_3^2 + \frac{1}{2}A_2A_3\cos(\alpha+\beta-\gamma)\\ =&A_0^2 + \frac{3}{4}A_2^2 + \frac{1}{2}A_3^2 + \frac{1}{2}A_2A_3\cos(2\pi|f_b - f'_{MW}(t)|t + \Phi)\end{aligned} \tag{3.18}$$

Here, Φ represents the combined phase lag. Assuming that the microwave source is operating at a constant, known frequency, any Doppler shift in the microwave frequency is determined from the recorded frequency.

$$|f_b - f'_{MW}(t)| = \left| f_b - \left(1 + \frac{2v(t)}{c}\right) f_{MW} \right| \tag{3.19}$$

This is illustrated in Figure 3.4 with a simple case. Assume that $f_1 = 100$ Hz, $f_2 = 65$ Hz, $f'_{MW} = 20$ Hz, $f_d = 17$ Hz, $A_0 = 0$, and $A_2 = A_3 = 1$. The frequencies here are in Hz to make the example easier to visualize, but holds true for the actual laser and microwave frequencies and detector bandwidth. The first laser's E field is shown in Figure 3.4 (i). This E field is modulated by the microwave beam using the EO crystal and polarization optics, giving the beat signal shown in Figure 3.4 (ii). The second laser's E field, which is shown in figure 3.4 (iii), is combined with the EO modulated signal. The combined E field of both

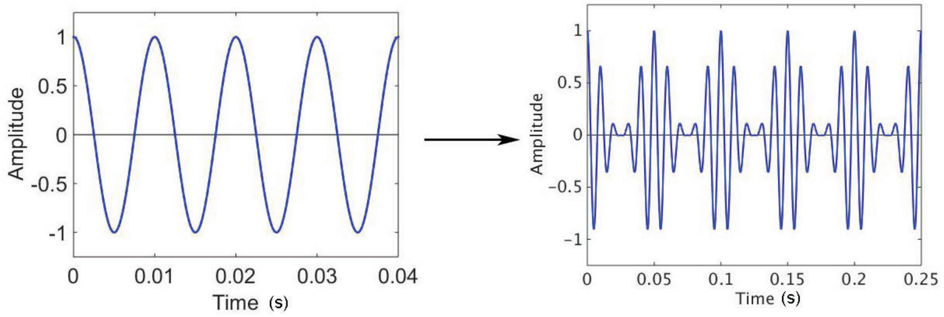

(i) Laser 1 at Frequency, f_1

(ii) Laser 1 Modulated by EO Crystal

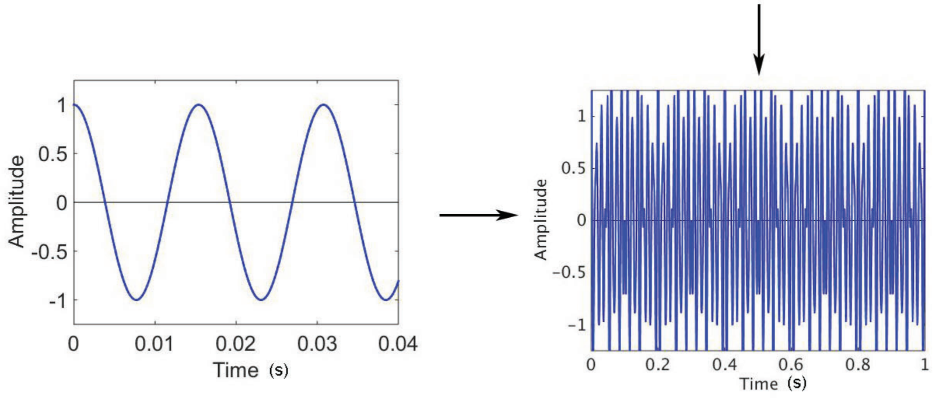

(iii) Laser 2 at Frequency, f_2

(iv) E Field of Combined Lasers

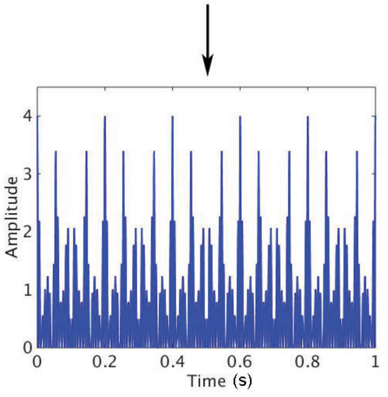

(v) Intensity Seen by Detector

Figure 3.4: Evolution of E fields through the MPMI concept.

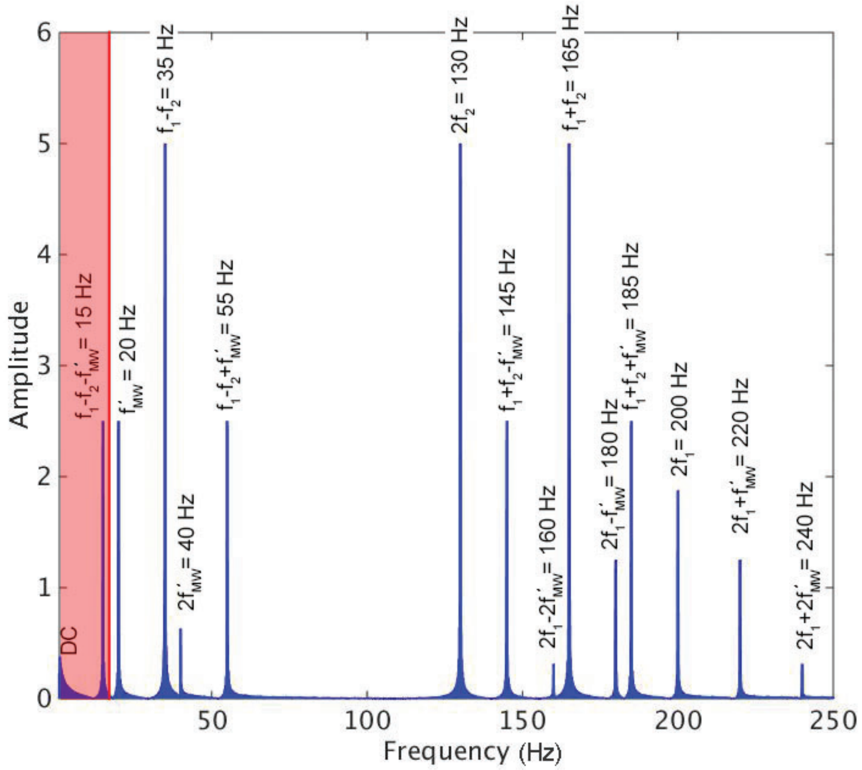

Figure 3.5: FFT of the intensity generated by the MPMI example showing all frequencies present. The detector bandwidth, shown in red, encompasses only the $|f_b - f'_{MW}|$ and DC signals.

lasers is shown by Figure 3.4 (iv), yielding the intensity shown in Figure 3.4 (v). A FFT on the intensity identifies the frequencies present, as shown in Figure 3.5. All of the frequencies in Equation 3.14 are seen in the FFT. However, only $|f_b - f'_{MW}|$ and the DC signals are within the detector bandwidth, identified by the red region. Changes in f'_{MW} due to surface motion result in a change in the recorded frequency.

The MPMI design assumes the laser beat and microwave frequencies are constant in time. Variations in the microwave frequency are not as large a concern. Typically, variations are under a kHz [27], resulting in a velocity error of a few m/s. Variations in the laser frequencies are often on the order of 10's of MHz [39, 38]. This is a significant source of error that needs to be accounted for with a reference channel. The generation of a reference channel involves splitting off a signal from each laser. A custom EO modulator imparts an amplitude modulation to one of the laser signals slightly above or below the microwave frequency before being combined with the other laser signal. This provides a measurable signal for the beat frequency in the same manner as the MPMI. This assumes the EO modulator has a constant, well-known modulating frequency. This was not done in this work due to time constraints, but is recommended for any future implementations. The issue of laser drift is eliminated completely by employing a single laser MPMI design. This interferometer design is described in Appendix B. In this design, the laser is sent through a commercial EO modulator operating near the microwave frequency before being modulated by the microwave source at the EO crystal. Imparting both modulations to the beam enables a measure of the microwave frequency. The advantages of the two laser concept is it allows for the detection of very weak modulated signals, several dB lower than the reference [19].

The ability to obtain multiple measurements over a moving surface with the MPMI is achieved through proper imaging. The microwave source can be collimated reasonably well (*i.e.* with a divergence angle of a few degrees) with a Gaussian lens [27] and directed towards the measurement surface. A dielectric or metal lens can image the reflected microwave signal to the EO crystal [22]. The laser reflected from the back surface of the EO crystal is then imaged onto a fiber array. If enough light is collected by each fiber in the array, multiple measurements result. Changing the imaging optics in the system and the arrangement of the fibers in the array alters the location and resolution of the measurements taken.

Chapter 4

Verification of the MPMI Operating Principle

Extracting the microwave frequency from the EO modulation of a laser beam is the fundamental operating principle of the MPMI concept and represents its main technical challenge. A series of experiments were constructed to quantify the ability of the MPMI design to accurately recover a microwave frequency. The MPMI concept presented in Figure 3.3 was modified by removing the microwave beamsplitter and directing the microwave source towards the EO crystal. This modification has the advantage of maximizing the amount of microwave power directed towards the EO crystal. A schematic of this configuration is shown in Figure 4.1. A photograph of the actual setup is shown in Figure 4.2. The experimental setup is discussed in four sections: laser characterization, EO crystal selection, detector selection and characterization, and optical configuration. Following that, the results of the experiments are presented and discussed. Alterations to increase the modulated signal strength are then proposed.

4.1 Experimental Configuration

4.1.1 Laser Characterization

For these experiments, two tunable 1550 nm lasers were used. A high-powered NP Photonics Rock$^{\text{TM}}$fiber laser capable of generating 2.2 W was used to generate the modulated beam (*i.e.* Laser 1). The high power level was used to increase the modulated signal strength sent to the detector. The reference laser (*i.e* Laser 2) was a 50 mW NKT Photonics Koheras ADJUSTIK fiber laser. A high power was not necessary for the reference laser, since it was completely contained in a fiber and did not experience the losses associated with coupling from an open beam. The Rock$^{\text{TM}}$laser was an older model and had a narrow tunable range, leading to only a few operational frequencies. The Rock$^{\text{TM}}$laser was kept in the same operating position, around 1550.15 nm, and the NKT laser was tuned around it to generate the desired beat frequency. Given the tunable range of the NKT laser, this limited

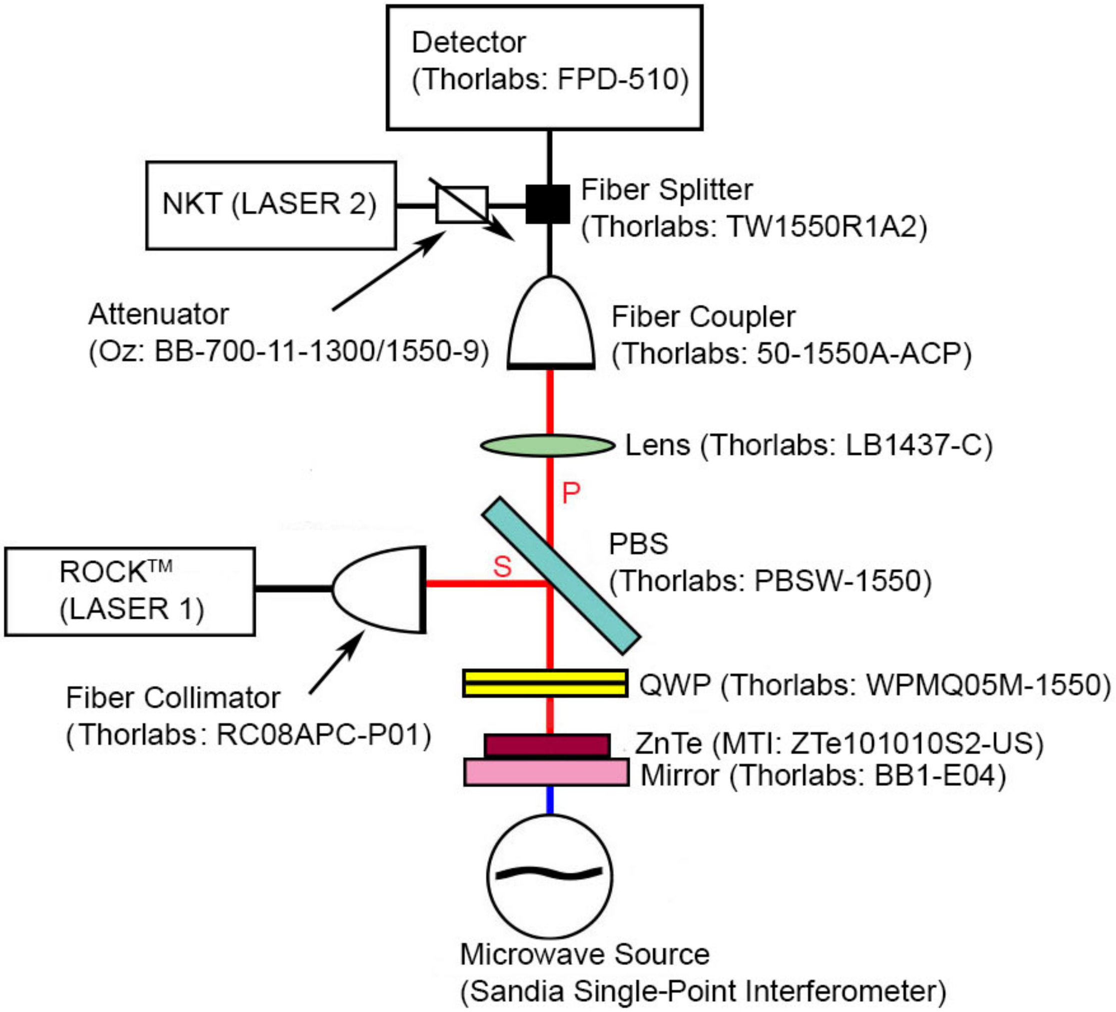

Figure 4.1: Schematic illustrating the MPMI design used to extract the microwave frequency from an EO modulated laser.

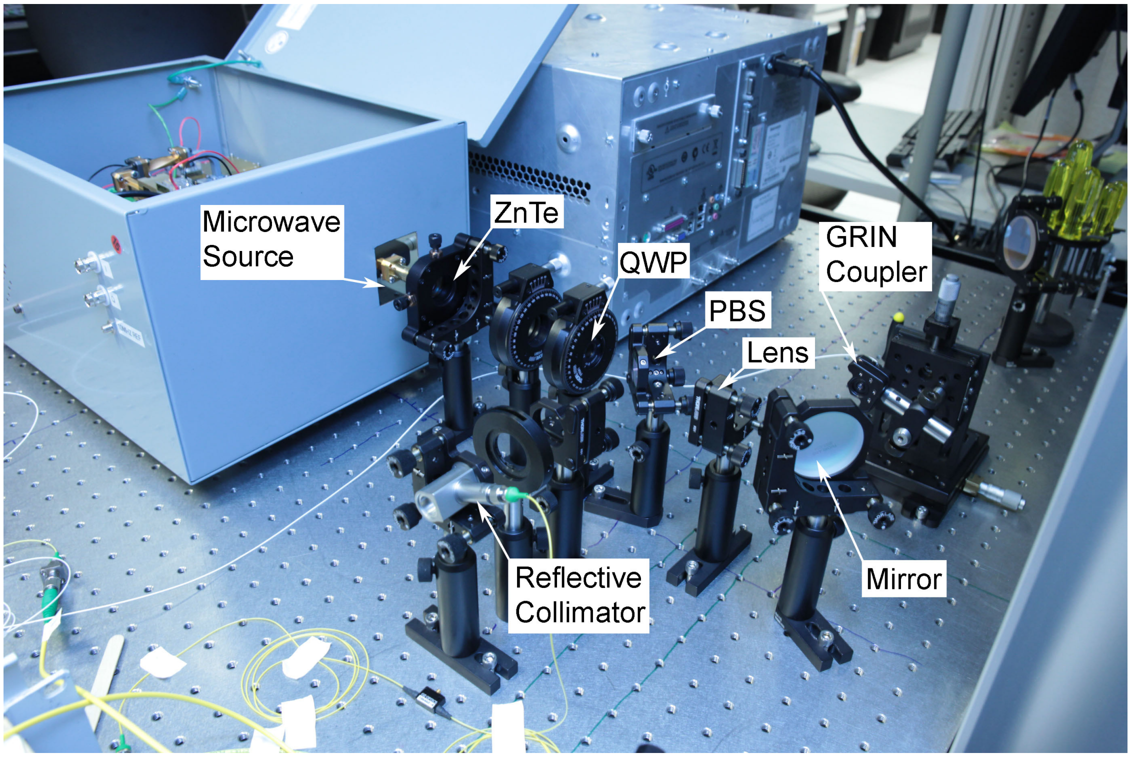

Figure 4.2: Photograph of the actual experimental setup.

the beat frequencies achievable to around 74 GHz, which was more than adequate for the 35.2 GHz source.

As previously discussed, the MPMI concept relies on the generation of a stable beat frequency between the two lasers. This is complicated by the inherent frequency drift present in each laser. Before each experimental set, the wavelengths of both lasers were measured with an Agilent 86122A Multi-Wavelength meter. These measurements provided insight into the frequency drift present. The Rock^{TM}laser was the least stable of the two, and tended to find a different operational range every time it was turned on. This necessitated measuring its wavelength upon start up and adjusting the NKT accordingly. Based on these measurements, the overall wavelength difference between the two lasers tended to have a maximum error of ± 0.2 pm. For a beat frequency of 35 ± 1 GHz, this corresponds to an error of ± 56 MHz. This was tested by setting the two lasers to beat at 25 MHz and recording the response with a Newport 1623 detector. Over these experiments, the measured beat frequency varied by ± 23 MHz. The laser drift manifested in changes to the beat frequency between measurements. Over the course of a single experiment (*i.e* 10 μs), the frequency remain within 30 kHz. This level frequency drift has a significant effect on the ability to extract a velocity, which is discussed in Section 4.3. For the purposes of extracting the microwave frequency from an EO modulated laser, the drift is less limiting and is only considered to ensure the modulated signal stays within the detector's range.

4.1.2 Electro-Optic Crystal Selection

While it is possible to use a polycrystalline EO material to modulate a laser [20], it is more efficient to use a single crystal. The crystallographic orientation determines which component of the electric field is visible [46]. While there are a large number of EO crystals [5], the one chosen for the MPMI must have high laser transparency, a large EO coefficient, and a small group velocity mismatch (GVM). The GVM quantifies the relative difference in speed between the microwave signal and the laser through the EO crystal. All of these requirements are necessary for terahertz spectroscopy [11], leading to a wealth of literature available to choose an EO crystal for the MPMI.

The indexes of refraction, EO coefficients, and approximate GVMs of several commonly used crystals in terahertz spectroscopy are presented in Table 4.1. These parameters are wavelength dependent, so it is common to find multiple values reported in the literature [5]. The parameters listed in Table 4.1 represent one reported value and are used as approximations to determine candidate crystals for the MPMI.

Table 4.1: Indexes of refraction, EO coefficients, and GVMs for several commonly used EO crystals [11, 48].

EO Crystal	EO Coefficient (pm/V)	GVM (ps/mm)
ZnTe	$r_{41} = 4.0$	1.1
CdTe	$r_{41} = 4.5$	0.75
ZnSe	$r_{41} = 2.0$	0.96
GaAs	$r_{41} = 1.4$	0.015
GaP	$r_{41} = 0.97$	-
GaSe	$r_{41} = 14.4$	0.1
$LiTaO_3$	$r_{33} = 30.5$	14.1
	$r_{13} = 8.4$	
$LiNbO_3$	$r_{33} = 30.9$	14.2
	$r_{51} = 32.6$	
DAST†	$r_{11} = 160$	1.2

†4-N,N-dimethylamino-4’-N’-methyl-stilbazolium tosylate

For the MPMI concept, a GVM around 1 ps/mm or less was desired. It is possible to compensate for a large GVM and phase match the two beams by sending the faster wave through the crystal at an angle [48]. However, this destroys the spatial resolution, and is not considered an option for the MPMI. Both $LiTaO_3$ or $LiNbO_3$ have too large a GVM for the MPMI concept. DAST is a soft brittle material that is hygroscopic, making it hard to get quality optical surfaces [30]. GaSe is cleaved easily and very fragile [11]. There is also less literature on these two crystals. It was decided to concentrate on the inorganic standards of ZnTe, ZnSe, and CdTe for the MPMI.

The applicability of each crystal considered depends on the laser and microwave frequencies utilized. The optical indexes of refraction for ZnTe, ZnSe, and CdTe from their transmission limit to 2500 nm was previously measured and fit a modified Sellmeier equation [25].

$$n_{opt}^2 = a_1 + \frac{a_2 \lambda^2}{(\lambda^2 - a_3^2)} \tag{4.1}$$

This index of refraction does not account for dispersion in the crystal, which is captured with the following expression [29].

$$n_{eff} = n_{opt} - \lambda \frac{dn_{opt}}{d\lambda} \tag{4.2}$$

In both these equations, λ is expressed in μm. The index of refraction of each crystal in the THz regime was also measured between 0.3 and 3 THz and fit to an empirical relation [17].

$$n_{THz}^2 = \frac{b_1 b_2^2 - b_3 f_{THz}^2}{b_2^2 - f_{THz}^2} \tag{4.3}$$

Here, f_{THz} is the frequency in THz. The coefficients for the index of refraction equations are listed in Table 4.2. The GVM, expressed in ps/mm, is calculated from these indexes of refraction.

$$GVM = \left| \frac{n_{THz}}{c_0} - \frac{n_{eff}}{c_0} \right| \times 10^9 \tag{4.4}$$

The coherency length, or maximum distance that the velocity mismatch is tolerable, is also calculable [29].

$$l_c = \frac{\pi c_0}{2\pi f \left| n_{eff} - n_{THz} \right|} \tag{4.5}$$

In this expression, f refers to the frequency in Hz.

Table 4.2: Coefficients for the index of refraction calculations [17, 25, 23].

EO Crystal	a_1	a_2	a_3^2 (μm^2)	b_1	b_2 (THz)	b_3
ZnTe	4.27	3.01	0.142	9.92	5.39	6.0
CdTe	5.68	1.53	0.366	10.20	4.23	7.1
ZnSe	4.00	1.90	0.113	8.99	6.09	5.3

The MPMI concept utilizes a 1550 nm laser and a 35.2 GHz microwave source. The indexes of refraction, GVMs, and the coherency lengths were determined for each crystal. In addition, a performance parameter, $n^3 r_{ij}$, was calculated. These values are listed in Table 4.3. While the index of refraction for the microwave beam is an extension of the fit given in Equation 4.3, it is assumed accurate enough to determine an EO crystal for the MPMI. From Table 4.3, CdTe is the best choice, followed by ZnTe. Both crystals have a Zinc Blend structure [11]. The (110) crystallographic orientation visualizes the in-plane components of the electric field, while the (100) orientation visualizes the out-of-plane components [46]. A 10 mm X 10 mm X 1mm (110) ZnTe crystal (MTI Corporation ZTe101010S2-US) was used in this work. A (110) CdTe crystal (MTI Corporation CdTee101010S2) was intended to be used, but fractured and a replacement could not be procured for the experiments.

Table 4.3: Comparison of EO crystals for the MPMI concept using a 1550 nm laser and a 35.2 GHz microwave source.

EO Crystal	n_{opt}	n_{eff}	n_{THz}	GVM (ps/mm)	l_c (mm)	$n^3 r_{ij}$ (pm/V)
ZnTe	2.733	2.899	3.150	0.84	17.1	97.5
CdTe	2.736	2.977	3.194	0.72	19.7	118.7
ZnSe	2.450	2.516	2.998	1.61	8.9	31.9

4.1.3 Detector Selection and Characterization

Choosing a detector involved the consideration of three variables: the bandwidth, the gain, and the dark noise. The bandwidth was touched on previously. It must be large enough to resolve the frequencies of interest given the expected frequency drift while still small enough to eliminate the unwanted frequencies. Based on Equation 3.19 and a 35.2 GHz source, a velocity of 8,000 m/s results in around a 2 MHz Doppler shift. The minimum bandwidth necessary is driven more by the expected frequency drift than the velocities recorded. A large gain is needed since the modulated signal strength is expected to be under 1 μW. Increases in the detector gain tend to increase the dark noise or lower the bandwidth. Careful balancing of these parameters is necessary.

The Thorlabs FPD 310 and FPD 510 detectors were considered for these experiments. The properties of each are listed in Table 4.4. The FPD 310 has a larger calculated gain, bandwidth, and dark noise than the FPD 510 [37]. The FPD 310 is also not recommended for continuous light applications [37].

Table 4.4: Parameters given by the manufacturer for the detectors considered [37].

Detector	Coupling	Frequency Range (MHz)	Calculated Gain (V/W)	Noise level (dBm)
FPD 310	AC	10-1800	5e4	-90
FPD 510	DC	0-250	4e4	-120

Recording the zero light response from both the FPD 310 and FPD 510, which is shown in Figure 4.3, visualizes the increased noise of the FPD 510. The dark noise was recorded with a 6 GHz, 25 GS/s oscilloscope (Tektronics DPO070604B). An FFT was generated with the Sandia Matlab AnalysiS Hierarchy (SMASH) toolbox [14] on the dark noise recordings

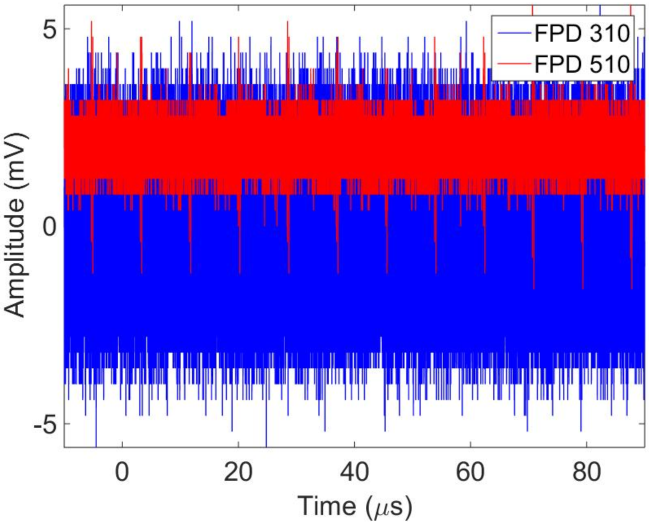

Figure 4.3: Recorded dark noise for both the FPD 310 (Blue) and FPD 510 (Red) detectors.

to identify any artificial frequencies. The FPD 310 had several artificial frequencies within its range: 333 MHz, 467 MHz, 600 MHz, 867 MHz, 1.00 GHz, 1.27 GHZ, 1.60 GHz, and 1.80 GHz. These are visualized in Figure 4.4a by peaks in the FFT response. The FPD 510 response, which is shown in Figure 4.4b, had no artificial frequencies over its bandwidth other than a DC signal.

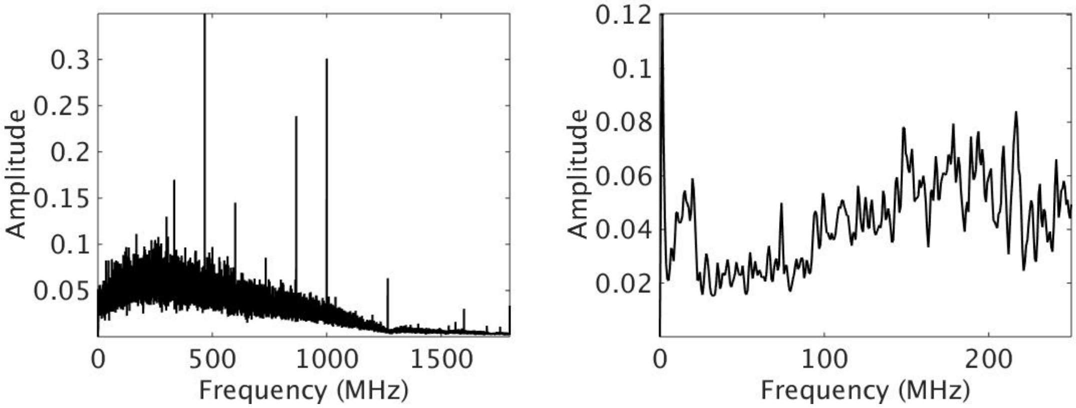

(a) FPD 310

(b) FPD 510

Figure 4.4: Mean response at each frequency in the detector ranges for both the FPD 310 (a) and FPD 510 (b). The peaks represent the artificial frequencies present.

The FPD 510 was chosen for extracting the microwave frequency from the EO modulation of a laser beam. The gain values reported in Table 4.4 are calculated and not the actual values for the detector. A series of measurements were performed to determine the actual

DC gain curve of the FPD 510. The results are given in Table 4.5. The gain is not constant and is maximized around 50 μW of power. For all experiments, the reference power was adjusted to ensure that roughly 50 μW was sent to the detector.

Table 4.5: Measured DC gain values for the FPD 510 detector.

Power (μW)	Gain (V/W)
1	3245
2	3437
5	4167
10	5762
30	10353
50	11364
70	9535
100	7136
200	3604
500	1431
1000	705

4.1.4 Optical Configuration

The output of the ROCK$^{\text{TM}}$laser was collimated into an open beam with a reflective collimator (Thorlabs RC08APC-P01), since it provided the best collimation output [2]. The ROCK$^{\text{TM}}$laser was connected to the reflective collimator with a fiber jumper that was bent to adjust the output polarization to maximize reflection at the PBS. A plate PBS (Thorlabs PBSW-1550) was chosen, since its extinction ratio (10,000:1) was higher than a PBS cube [37]. A large extinction ratio reduces bleed through, which is the A_0 term in Equation 3.18 and represents signal noise. In the current system, the bleed through was approximately 4 μW of power. After reflection from the PBS, the light was directed through a multi-order QWP (Thorlabs WPMQ05M-1550). The QWP was placed in a precision rotation mount (Thorlabs PRM1) for increased control of its alignment. The light passed through the ZnTe crystal, which was mounted onto a dielectric mirror (Thorlabs BB1-E04) with double-sided tape and placed in a 6 axis mount (Thorlabs K6XS). The 6 axis mount enabled proper alignment of the crystal with the ability to rotate its orientation.

After modulation by the EO crystal, a small signal was transmitted through the PBS. This transmitted signal was focused using a bi-convex lens with a focal length of 150 mm (Thorlabs LB1437-C) into a gradient-index (GRIN) fiber coupler (Thorlabs 50-1550A-APC). The GRIN coupler gave better coupling back into the fiber, around 6%, than the other couplers considered. Even with the GRIN fiber coupler, coupling back into the fiber represented a significant loss in the system. The modulated beam and the reference signal were combined with a 99:1 fiber splitter (Thorlabs TW1550R1A2), maximizing the amount of modulated signal sent to the detector. The NKT reference laser output was sent through a fiber attenuator (Oz Optics BB-700-11-1300/1550-9/125-S-60-3A3A-1-1) before the fiber splitter to enable fine adjustment its power.

It is important to note that the ZnTe crystal used was not anti-reflective (AR) coated, due to time constraints. At 1550 nm, the transmission of ZnTe is around 60% [32]. This meant there were multiple reflected signals transmitted through the PBS, representing reflections from the initial ZnTe surface, the mirror surface, and numerous internal reflections. An AR coating on the ZnTe surface would reduce these multiple reflected signals and increase the modulated signal strength. For these experiments, care was taken to couple just the signal reflected from the mirror back into the fiber. An AR coating on the EO crystal's front side is recommended for any future implementations. A HR coating on the back side of the EO crystal is also recommended to eliminate the dielectric mirror.

4.2 Experimental Procedure and Optimization of the EO Crystal's Orientation

With the components selected and characterized, the next step was to determine the optimal orientation of the ZnTe crystal. This occurs when the crystal's fast axis is 45^o to the input light's polarization direction, producing the maximum possible phase lag. The optimal ZnTe orientation was found by systematically rotating the crystal between experiments. Due to the symmetry of the crystal, only a 45^o angular range was investigated. Initially, nine experiments were performed at 5^o increments from the crystals original orientation.

First, the wavelength of each laser was measured with the Agilent wavelength meter, and the NKT reference laser was tuned to provide the desired beat frequency. Once the lasers were set, the GRIN fiber coupler was aligned to maximize coupling back into the fiber. This was accomplished by rotating the QWP to maximize the signal transmitted through the PBS. The alignment of the GRIN coupler was adjusted to maximize the power collected, which was measured with a Newport 1918-R power meter with a Newport 818-IR detector. Due to the 25 mW power limit of the Newport power meter, this was done with only the ROCK$^{\text{TM}}$laser at 120 mW of power. The QWP was then rotated to generate as little transmitted power as possible, which was measured at the output of the GRIN coupler with the Newport power meter. In minimizing the transmitted signal, the ROCK$^{\text{TM}}$laser's power was increased to its maximum of 2.2 W. The total bleed through was between 2 and 6 μW for all experiments. The power of the NKT reference laser sent to the FPD 510 detector was adjusted with the fiber attenuator. Based on the gain curve presented in Section 4.1.3, the reference laser strength was set to 50 μW, which was measured at the output of the fiber splitter with the Newport power meter. Finally, the output of the microwave source was placed directly behind the dielectric mirror. Based on the specifications of the microwave components, it is estimated that around 100 mW of power reach the ZnTe crystal.

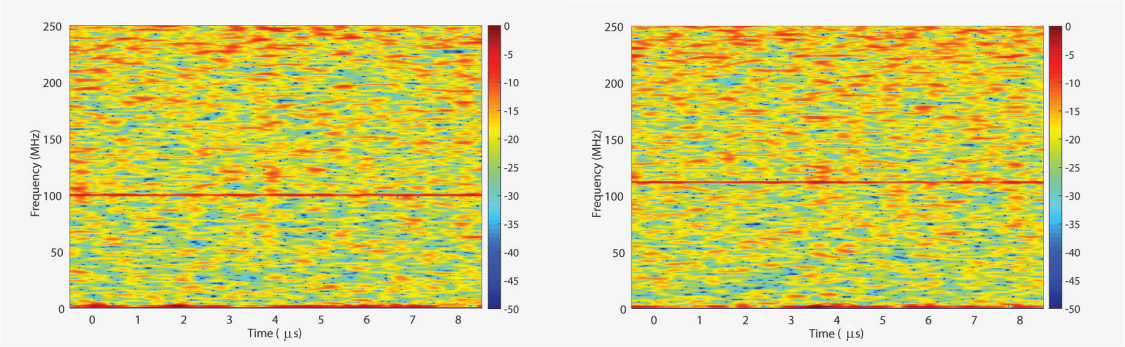

(a) Exp. 1 (b) Exp. 2

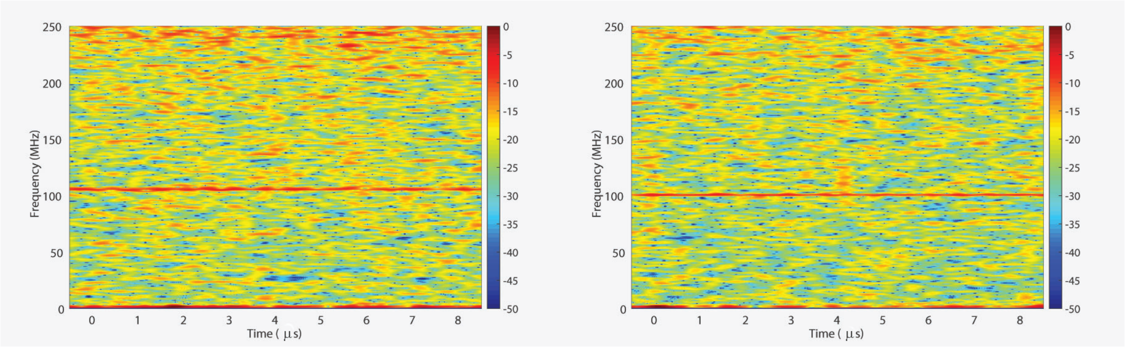

(c) Exp. 3 (d) Exp. 4

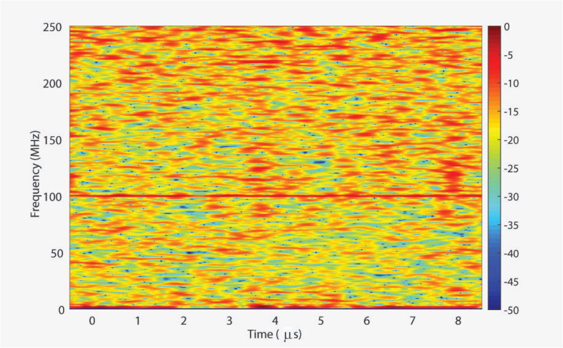

(e) Exp. 5

Figure 4.5: FFT spectra showing the difference between the beat and microwave frequencies for a (110) ZnTe crystal.

Table 4.6: Experimental results for a (110) ZnTe crystal.

Experiment	Recorded Frequency (MHz)
1	99.57 ± 1.04
2	111.42 ± 1.46
3	106.12 ± 2.33
4	100.13 ± 0.97
5	99.69 ± 2

For each orientation, three measurements were recorded on a 6 GHz, 25 GS/s oscilloscope (Tektronics DPO070604B). The record signals were analyzed with the SMASH [14] toolbox, using 1000 blocks, an overlap of 100, 16384 frequency points, a Gaussian window, and DC removal. The results of the initial experiments showed a faint response for the 5^o, 10^o, and 15^o orientations that was out of the detector's specified range. For these experiments, it was erroneously believed that the microwave source was operating at 35 GHz as specified by the manufacturer. A new series of experiments was performed to further investigate this angular range.

A series of 5 experiments were performed on angles ranging between 5^o and 15^o, using the same procedure as outlined above. The frequency signals were higher than expected again, but within the detector's range. The results suggested that the 10^o orientation was optimal and that the source was 200 MHz higher than the manufacturer's specification. This was not identified in the verification tests presented in Section 2.2, since it represents roughly a 0.5% error. The single-point results were redone once the discrepancy was identified.

Five measurements were taken at an orientation of 10^o. The ROCK$^{\text{TM}}$and NKT lasers' wavelengths were measured as 1550.1527 nm and 1550.4358 nm, respectively. This generated a laser beat frequency of 35.313 GHz. The results were analyzed in SMASH [14] with the same parameters and are presented in Table 4.6. The FFT spectra are shown in Figure 4.5. The difference between the beat and microwave frequencies are clearly visible in the FFT spectra and prove the underlying physical principle of the MPMI concept.

4.3 Discussion of the Experimental Results

While the EO modulation experiments presented in Table 4.6 proved the extraction of a microwave frequency with the MPMI concept, they also highlighted the challenges that manifest at the lower microwave frequency. In the microwave regime, Doppler shifts are on the order of kHz. The modulated frequency needs to be extracted to a high degree of accuracy, much more than in optical methods where Doppler shifts are on the order of GHz. At 35.2 GHz, a 1 MHz frequency error represents a velocity uncertain of roughly

4000 m/s. The frequency error in the experiments presented is on the order of 2 MHz. That corresponds to a velocity uncertainty around 8000 m/s, precluding the measurement of any practical velocity. This limits the applicability of the diagnostic with the equipment currently employed.

It is possible to decrease the frequency uncertainty. The incorporation of a reference channel to monitor the beat frequency of the lasers, as discussed in Section 3.2, is an option. As stated in Section 4.1.1, the drift in the beat frequency over the course of a typical experiment (*i.e.* 10 μs) is around 30 kHz. At 35.2 GHz, this corresponds to a velocity error of 130 m/s. This is not the only factor in the frequency error, so it is unlikely that such a large improvement is achievable with just a reference channel.

The low modulated signal strength plays a significant role. The frequency uncertainty, Δf, of any signal processed with a FFT depends on the sampling rate, f_s, signal noise fraction, σ, and FFT window, τ [13].

$$\Delta f = \left(\sqrt{\frac{6}{f_s}} \frac{\sigma}{\pi} \right) \tau^{-\frac{3}{2}} \tag{4.6}$$

This quantifies the signal noise as largest obstacle to the successful implementation of the MPMI. The modulated signal was orders of magnitude below the reference leg, producing a large noise fraction. This necessitates a large time window to obtain the adequate frequency uncertainty, eliminating the MPMI from many experimental configurations.

This was illustrated by extracting the microwave frequency over a time span of 100 μs. For these experiments, the Rock$^{\text{TM}}$and NKT lasers were operating at wavelengths of 1550.1527 nm and 1550.4358 nm, respectively. This corresponded to a beat frequency of 35.313 GHz. The results were analyzed using SMASH [14] with the same parameters listed in Section 4.2, effectively increasing the time window, τ, of the FFT. The results of these experiments are listed in Table 4.7, with a representative FFT spectrogram shown in Figure 4.6a. The longer time window reduced the frequency error to around 250 kHz, which produces a velocity error around 1000 m/s. Running the FFT with 100 time blocks and an overlap of 10, which is also listed in Table 4.7, dropped the frequency uncertainty to around 22 kHz. A representative FFT spectrogram is shown in Figure 4.6b. This produces a velocity error around 90 m/s, but a temporal resolution around 1 μs. Such a large timescale severely limits the applicability of the MPMI for studying energetic media.

The low modulated signal strength is the limiting factor in obtaining an accurate velocity. Using Equation 4.6, the signal noise fraction in these experiments was around 4.5. Improving the modulated signal strength is the main remaining technical challenge. Without more modulated signal strength, it is not possible to measure multiple velocities. It took collecting as much of the modulated signal as possible to obtain a single measurement of the frequency difference. While the MPMI concept is viable, a substantial investment in equipment is necessary to make it a reality.

Table 4.7: Experimental results with a time span of 100 μs.

Experiment	Time Blocks	Recorded Frequency (MHz)
1	1000	114.16 ± 0.31
	100	114.14 ± 0.022
2	1000	109.75 ± 0.24
	100	109.75 ± 0.022
3	1000	103.72 ± 0.31
	100	103.65 ± 0.021

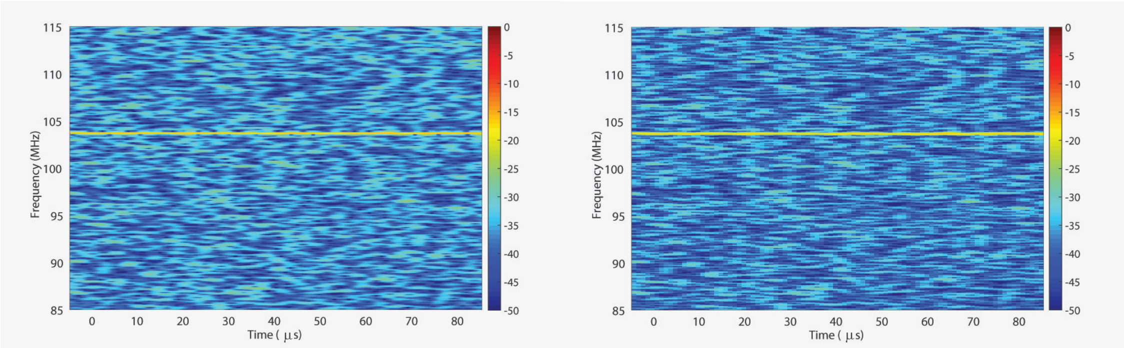

(a) 1000 Time Blocks

(b) 100 Time Blocks

Figure 4.6: FFT spectra showing the results with a 100 μs time window using both 1000 time blocks (a) and 100 time blocks (b). The images are zoomed in to clearly show the frequency response.

4.3.1 Alterations Necessary for Measuring Multiple Velocities

While the underlying principle of the MPMI concept was proven, the equipment necessary to accurately measure a velocity was not available. The knowledge gathered through the course of the project has identified several avenues for developing a working MPMI by obtaining a stronger modulated signal. It is likely that alterations in all areas discussed are necessary to obtain multiple velocity measurements.

One improvement is increasing the oscilloscope sampling rate. That reduces the frequency error per Equation 4.6. It also increases the computational resources necessary to analyze the data. Increasing the microwave power is another obvious alteration. Higher microwave power increases the phase lag generated, increasing the modulated signal strength. A 94 GHz source was available for this project capable of generating a 2 inch diameter beam with over 1 W of total power. Even this increase in signal strength is not enough to measure a velocity, especially considering the 75% reduction in power generated by two passes through a 50:50 beam splitter. Additionally, there are losses generated by the material imaged through and the interface reflectivity. It is likely that a multiple W source is necessary, posing some safety concerns. To avoid a high power microwave source, it is possible to use a crystal with a higher EO coefficient. The experiments in this work used ZnTe, since it is a well-established standard in terahertz spectroscopy [11]. Switching to DAST provides a substantial improvement in the modulated signal strength. With a 1 cm thick DAST crystal, a near 400× increase in the phase lag is generated compared to ZnTe. That increase in modulated signal strength may enable multiple measurements.

Another option to increase the modulated signal strength is more laser power. Increasing the laser power is a more complicated change. Without a larger extinction ratio in the PBS, increasing the laser power increases the bleed through at the PBS. This may lead to saturation of the detector, especially if the gain is increased. Increased detector gain is desired, since it lowers the reference power needed and, as a result, the signal noise fraction. A means to keep the laser power lower is to improve the coupling efficiency back into the fiber and apply an AR coating to the EO crystal. An AR coating would limit loses at the EO crystal/air interface. Additionally, better optical focusing would improve the 6% coupling efficiency of the GRIN coupler. Once again, that improvement may need a larger extinction ratio on the PBS to ensure the detector is not saturated. Ideally, it is desirable to have as large a laser power, PBS extinction ratio, detector gain, and fiber coupling as possible. Unfortunately, the interdependence of these parameters necessitates careful consideration.

Chapter 5

Summary and Conclusions

A single-point microwave interferometry capability was reestablished at Sandia. A 35.2 GHz interferometer was designed and constructed. Its application was verified through the recording of a known surface velocity. A GUI-based analysis program was written in MATLAB® for quickly analyzing the data through peak counting, quadrature analysis, and a simple FFT. The knowledge gained from the implementation of the single-point interferometer was applied to the generation of a viable MPMI concept. The MPMI concept relied on an EO crystal to impart a phase modulation on a laser beam, effectively transferring the microwave frequency onto the laser. This phase modulation was converted into an amplitude modulation through the use of polarization optics. This information transfer eliminated the challenges associated with collimating a microwave beam over large distances and recording it on time scales necessary for shock physics experimentation. A simplified version of the MPMI concept was constructed to measure a microwave frequency through the EO modulation of a laser beam. These experiments proved the underlying physical principle of the MPMI concept. However, they illustrated that the longer microwave wavelength imposed practical limitations on such a diagnostic. Given the equipment available, the recorded experimental results contained too large a frequency error to adequately measure a velocity. Alterations to the experimental setup to improve the modulated signal strength were discussed. These alterations centered on the microwave power, the laser power, the PBS extinction, the crystal's EO coefficient, the coupling efficiency back into the fiber, the detector gain, and the oscilloscope sampling rate.

References

[1] T. Ao and D. Dolan. SIRHEN: a data reduction program for photonic Doppler velocimetry measurements. Technical Report SAND2010-3628, Sandia National Laboratories, 2010.

[2] Tommy Ao. Personal Communication, 2015.

[3] L. Barker and R. Hollenbach. Laser interferometer for measuring high velocities of any reflecting surface. *Journal of Applied Physics*, 43(11):4669–4675, 1972.

[4] V. Bel'skii, A. Mikhailov, A. Rodionov, and A. Sedov. Microwave diagnostics of shock-wave and detonation processes. *Combustion, Explosion, and Shock Waves*, 47(6):639–650, 2011.

[5] A. Bhalla, W. Cook, R. Hearmon, J. Jerphagnon, S. Kurtz, S. Liu, D. Nelson, and J. Oudar. Landolt-Börnstein - group III: Crystal and solid state physics. In K. Hellwege and O. Madelung, editors, *Elastic, Piezoelectric, Pyroelectric, Piezooptic, Electrooptic Constants and Nonlinear Dielectric Susceptibilities of Crystals*, volume III/11. Springer-Verlag, Berlin, 1984.

[6] D. Bloomquist and S. Sheffield. ORVIS, optically recording velocity interferometer system, theory of operation and data reduction techniques. Technical Report SAND82-2918, Sandia National Laboratories, 1983.

[7] M. Cappelli, W. Hermann, M. Kodiak, N. Gascon, and W. Hargus Jr. A 90-GHz phase-bridged interferometer for plasma density measurements in the near field of a Hall thruster. In *2004 AIAA Joint Propulsion Conference*, page 3775. AIAA, 2004.

[8] R. Cole. High pressure solid propellant combustion studies using a closed bomb. Technical Report S-68, Rohm and Haas Company: Redstone Arsenal Research Division, 1965.

[9] M. Cook, R. Doran, and G. Morris. Measurement of detonation velocity by Doppler effect at three-centimeter wavelength. *Journal of Applied Physics*, 26(4):426–428, 1955.

[10] W. Culshaw. The Michelson interferometer at millimetre wavelengths. *Proceedings of the Physical Society B*, 63:939–954, 1950.

[11] S. Dexheimer. *Terahertz Spectroscopy Principles and Applications*, chapter Nonlinear Optical Techniques for Terahertz Pulse Generation and Detection - Optical Rectification and Electrooptic Sampling. CRC Press, Hoboken, 2007.

[12] D. Dolan. Foundations of VISAR analysis. Technical Report SAND2006-1950, Sandia National Laboratories, 2006.

[13] D. Dolan. Accuracy and precision in photonic Doppler velocimetry. *Review of Scientific Instruments*, 81(053905), 2010.

[14] D. Dolan, T. Ao, and J. Brown. Sandia Matlab AnalysiS Hierarchy. SAND Report, In preparation, 2015.

[15] C. Domier, W. Peebles, and N. Luhmann Jr. Millimeter-wave interferometer for measuring plasma electron density. *Review of Scientific Instruments*, 59(8):1588–1590, 1988.

[16] B. Glancy and A. Krall. Microwave interferometric measurements of particle and wave velocities in porous media. Technical Report NSWC TR 88-362, Naval Surface Warfare Center, 1990.

[17] T. Hattori, Y. Homma, and A. Mitsuishi. Indicies of refraction of ZnS, ZnSe, ZnTe, CdS, and CdTe in the far infarred. *Optics Communications*, 7(3):229–232, 1973.

[18] E. Hecht. *Optics*. Addison-Wesley, Reading, Massachusetts, 1987.

[19] D. Holtkamp. Survey of optical velocimetry experiments-application of PDV, a heterodyne velocimeter. In *2006 International Conference on MegaGauss Magnetic Field Generation and Related Topics*, pages 119–128. IEEE, 2008.

[20] J. Holzman, F. Vermeulen, S. Irvine, and A. Elezzabi. Free-space detection of terahertz radiation using crystalline and polycrystalline ZnSe electro-optic sensors. *Applied Physics Letters*, 81(12):2294–2296, 2002.

[21] E. Johnson. A microwave technique for studying detonation phenomena. Technical Report S-87, Rohm and Haas Company: Redstone Arsenal Research Division, 1965.

[22] W. Kock. Metal-lens antennas. *Proceedings of the Institute of Radio Engineers*, 34(11):828–836, 1946.

[23] A. Manabe, A. Mitsuishi, and H. Yoshinaga. Infrared lattice reflection spectra of II-VI compounds. *Japanese Journal of Applied Physics*, 6(5):593–600, 1967.

[24] Y. Maron and A. Blaugrund. Measurements of high surface velocities using K-band microwave interferometry. *Review of Scientific Instruments*, 51(5):666–669, 1980.

[25] D. Marple. Refractive index of ZnSe, ZnTe, and CdTe. *Journal of Applied Physics*, 35(3):539–542, 1964.

[26] G. McCall, W. Bongianni, and G. Miranda. Microwave interferometer for shock wave, detonation, and material motion measurements. *Review of Scientific Instruments*, 56(8):1612–1618, 1985.

[27] Millitech. Personal Communication, 2015.

[28] T. Moss, G. Burrell, and B. Ellis. *Semiconductor Opto-Electrics*. Wiley, New York, 1973.

[29] A. Nahata, A. Weling, and T. Heinz. A wideband coherent terahertz spectroscopy system using optical rectification and electro-optic sampling. *Applied Physics Letters*, 69(16):2321–2323, 1996.

[30] Y. Namba, M. Tsukahara, A. Fushiki, K. Suizu, and H. Ito. Single-point diamond turning of DAST crystals. In *Optical Manufacturing and Testing V*, volume 5180. SPIE, 2003.

[31] G. Neumann, U. Bänziger, M. Kammeyer, and M. Lange. Plasma-denisty measurements by microwave interferometry and Langmuir probes in an RF discharge. *Review of Scientific Instruments*, 64(1):19–25, 1993.

[32] T. Potlog, N. Maticiuc, A. Mirzac, P. Dumitriu, and D. Scortescu. Structural and optical properties of ZnTe thin films. In *2012 International Semiconductor Conference (CAS)*, volume 321-324. IEEE, 2012.

[33] K. Sasagawa, A. Kanno, T. Kawanishi, and M. Tsuchiya. Live electrooptic imaging system based on ultraparallel photonic heterodyne for microwave near fields. *IEEE Transaction on Microwave Theory and Techniques*, 55(12):2782–2791, 2007.

[34] K. Sasagawa, A. Kanno, and M. Tsuchiya. Real-time digital signal processing for live electro-optic imaging. *Optics Express*, 17(18):15641–15651, 2009.

[35] K. Sasagawa and M. Tsuchiya. Modulation depth enhancement for highly sensitive electro-optic RF near-field measurement. *Electronics Letters*, 42(23), 2006.

[36] P. Specht, M. Cooper, and B. Jilek. Design of a multi-point microwave interferometer using the electro-optic effect. In R. Chau, T. Germann, and T. Sewell, editors, *Shock Compression of Condensed Matter 2015*, page In Print. AIP, 2016.

[37] Thorlabs Product Specification. http://www.thorlabs.us/, 2015.

[38] NKT Photonics ADJUSTIK Laser Specifications. http://www.nktphotonics.com/product/koheras-adjustik-low-noise-single-frequency-lasers/, 2015.

[39] NP Photonics Rock$^{\text{TM}}$ Laser Specifications. http://www.npphotonics.com/images/pdfs/products/11_NPP_RockHPLS.pdf, 2015.

[40] P. Stanton, E. Venturini, and R. Dietzel. Microwave interferometer techniques for detonation study. Technical Report SAND85-1928C, Sandia National Laboratories, 1985.

[41] L. Strand, K. Magiawala, and R. McNamara. Microwave measurement of the solid-propellant pressure-coupled response function. *Journal of Spacecraft*, 17(6):483–488, 1980.

[42] L. Strand and R. McNamara. A variable-frequency driver-microwave transient regression rate measurement system. In *AIAA 14th Aerospace Sciences Meeting*, pages 155–172. AIAA, 1976.

[43] L. Strand, A. Schultz, and G. Reedy. Microwave Doppler shift technique for determining solid propellant transient regression rates. *Journal of Spacecraft*, 11(2):75–83, 1974.

[44] O. Strand, L. Berzins, D. Goosman, W. Kuhlow, P. Sargis, and T. Whitworth. Velocimetry using heterodyne techniques. In D. Paisley, S. Kleinfelder, D. Snyder, and B. Thompson, editors, *26th International Congress on High-Speed Photography and Photonics*, volume 5580, pages 593–599. SPIE, Alexandria, VA, 2004.

[45] M. Tsuchiya, T. Hashiba, and T. Shiozawa. Visual observation of characteristic behavior of RF waves in CRLH-TLs and their applications to dispersion characterizations. *IEEE Transaction on Microwave Theory and Techniques*, 58(12):4094–4101, 2010.

[46] M. Tsuchiya, K. Sasagawa, A. Kanno, and T. Shiozawa. Live electrooptic imaging of W-band waves. *IEEE Transaction on Microwave Theory and Techniques*, 58(11):3011–3021, 2010.

[47] O. Tudisco, A. Fabris, C. Falcetta, L. Accatino, R. De Angelis, M. Manente, F. Ferri, M. Florean, C. Neri, C. Mazzotta, D. Pavarin, F. Pollastrone, G. Rocchi, A. Selmo, L. Tasinato, F. Trezzolani, and A. Tuccillo. A microwave interferometer for small and tenuous plasma density measurements. *Review of Scientific Instruments*, 84(033505), 2013.

[48] Q. Wu and X. Zhang. Ultrafast electro-optic field sensors. *Applied Physics Letters*, 68(12):1604–1606, 1996.

Appendix A

Microwave Analysis Program (MWAP)

A Microwave Analysis Program (MWAP) was written in MATLAB® to quickly analyze data from a microwave interferometer using peak counting, quadrature analysis, and a simple fast Fourier transform (FFT). The MWAP program is still developmental. A more in depth quadrature analysis program, PointVISAR [14], and FFT analysis program, SIRHEN [1], are applicable to microwave interferometer data. Both of these programs are available through the SMASH package [14]. The SMASH package also includes more advanced FFT methods than SIRHEN [14]. The FFT method programed in the MWAP is very rudimentary. It was coded to make sense of data that has multiple overlaying frequencies. Below is a brief description of the program's operation. No in depth details are given about the numerical methods employed.

A.0.1 MWAP Operation

The folder containing the underlying m-files of the MWAP program should be added to the MATLAB® path. This enables operation of the program in any folder. The program automatically changes the working directory so all output files are saved with the data. The MWAP program is launched in the command window by typing *MWAP*, generating the load screen seen in Figure A.1. The data files to analyze are found with a file browser by clicking the **...** buttons. The **Load** button imports either a single channel or both channels into the memory for analysis. If only one channel is imported, all analysis screens have a single axis and only show the options available for that channel. Additionally, quadrature analysis is not available. In the present example, two signals are imported to show all the program's capabilities.

After loading in the desired data channels, the Signal Processing screen, shown in Figure A.2, appears. The loaded profiles are smoothed using a simple mean filter manually or with the slide bar. The window width is expressed as a percent of the signal. The default window for smoothing is 1%. The maximum window allowable is 10%. Any DC offset in the signals is also removable by fitting the data to a polynomials and subtracting them from the signals.

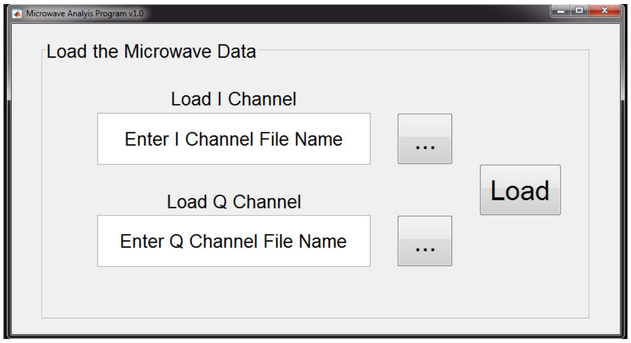

Figure A.1: MWAP Load screen.

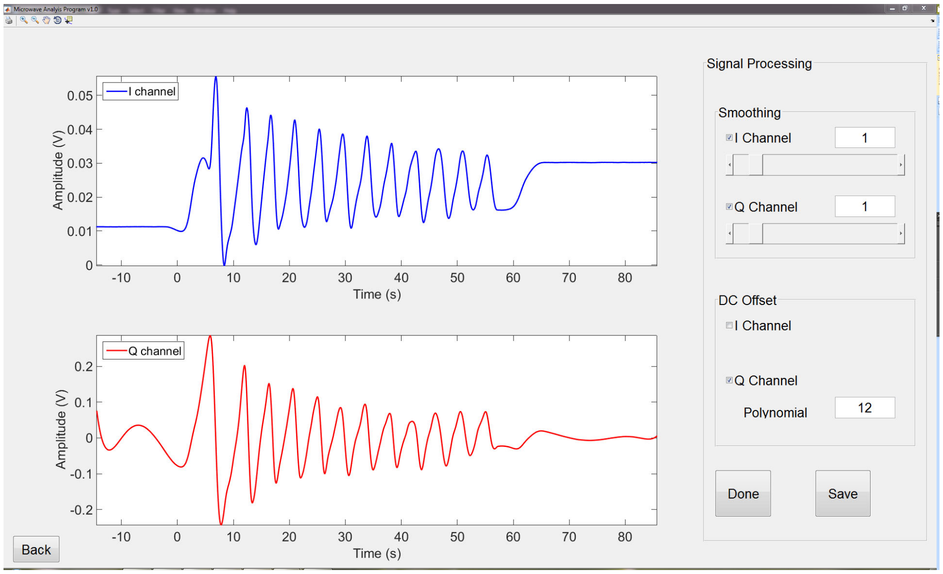

Smoothing
☑ I Channel 1
☑ Q Channel 1

DC Offset
☐ I Channel
☑ Q Channel
Polynomial 12

Figure A.2: MWAP Signal Processing screen.

The degree of the polynomial is adjusted with the text box. The **Save** button in the right corner launches the Save screen, shown in Figure A.3, for saving the processed signals as images and text files. The **File Identifier** changes the file name of the saved data.

After processing the signals, the **Done** button launches the Peak Finding screen, shown in Figure A.4. On this screen, a region of interest (ROI) is specified. This is done manually or by selection from the plot. Once a ROI interest is selected, black lines appear on the graph to indicate its location. The ROI is the whole signal by default. The program locates the maxima and minima in the ROI with two methods: the maximum absolute value of the signal between two zero points (Option **Maxima**) or from a quadratic fit to the signal between two zero points (option **Quadratic**). The **Maxima** method is the default, since it is the most robust. In order to locate the peaks, the code identifies a starting point in the ROI. This is done automatically by default (option **Automatic**) and is appropriate for most cases. Manual selection from the graph (option **Manual**) is available if the default method

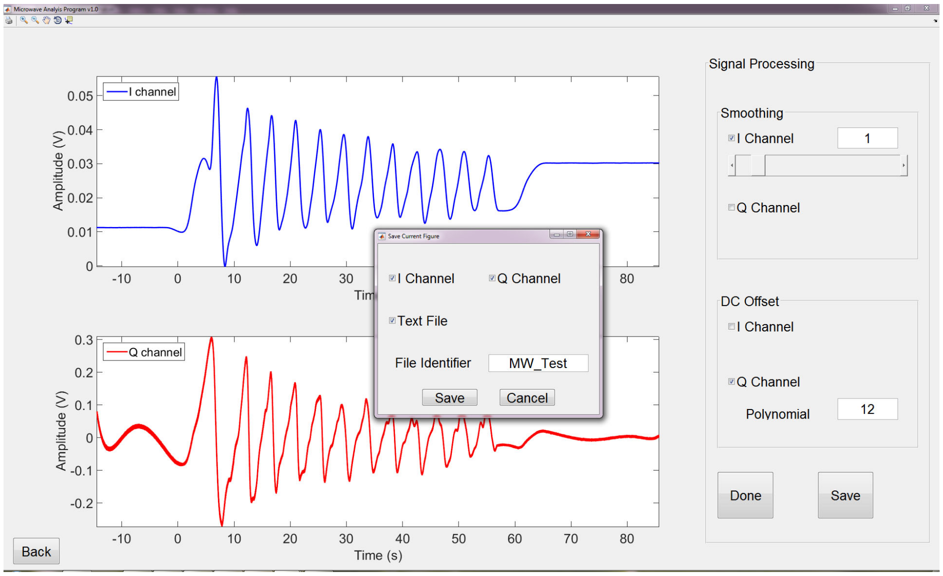

Signal Processing

Smoothing

☑ I Channel 1

☐ Q Channel

DC Offset

☐ I Channel

☑ Q Channel

Polynomial 12

☑ I Channel ☑ Q Channel

☑ Text File

File Identifier MW_Test

Figure A.3: MWAP Save screen.

fails. The starting point, maxima, and minima are visualized on the signal with red, black, and green dots, respectively.

Manual selection or modification of the maxima and minima is available with the **Modify** button. This generates the Peak Modifying screen, shown in Figure A.5. Selection of a point on the graph not near an established maxima or minima, adds one. Selection of a point on the graph near an established maxima or minima, deletes it. The **Done** box in the lower left corner moves back to the Peak Finding screen.

After the peaks are located, the **Done** button launches the Analysis Methods screen. Three methods are possible: peak counting, quadrature, or FFT. The peak counting method is the default, and its analysis screen is shown in Figure A.6. First, the necessary interferometer and material parameters are entered: the interferometer frequency and its drift over the experiment, the relative permittivity of the sample and its associated error, and the phase and mixer error of the interferometer. The default values are for the 35.2 GHz interferometer, detailed in Section 2.2, measuring through air. The peak counting is done with either the maxima or minima (*i.e.* points every half wavelength) or both (*i.e.* points every quarter wavelength). The distance versus time points for the selected options are displayed on the graph, with the slope in the upper left corner. The slopes are color coded with the position markers. The displacement data is saved as a figure or as a text file using the **Save** button. The saved figures differ from that displayed in that they include error bars on the distance markers and an error in the slope annotation in the upper left corner.

The Quadrature Analysis screen is shown in Figure A.7. The normalized I and Q signals are immediately plotted on the graph. The Lissajou is plotted by selecting the **Show Lissajou** option. The **Plot** button displays the distance versus time graph, shown in Figure

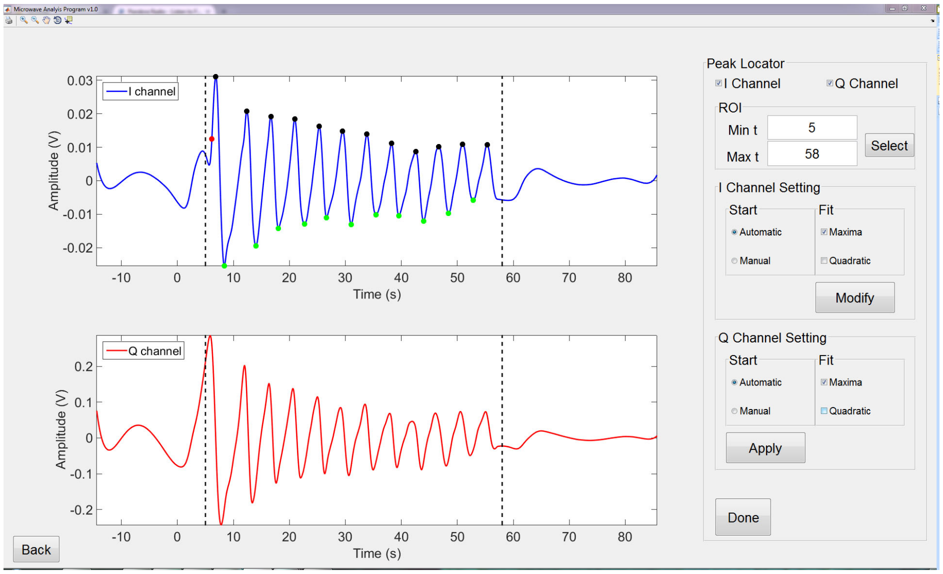

Peak Locator

☑ I Channel ☑ Q Channel

ROI

Min t: 5

Max t: 58

I Channel Setting

Start: ● Automatic ○ Manual

Fit: ☑ Maxima ☐ Quadratic

Q Channel Setting

Start: ● Automatic ○ Manual

Fit: ☑ Maxima ☐ Quadratic

Figure A.4: MWAP Peak Finding screen.

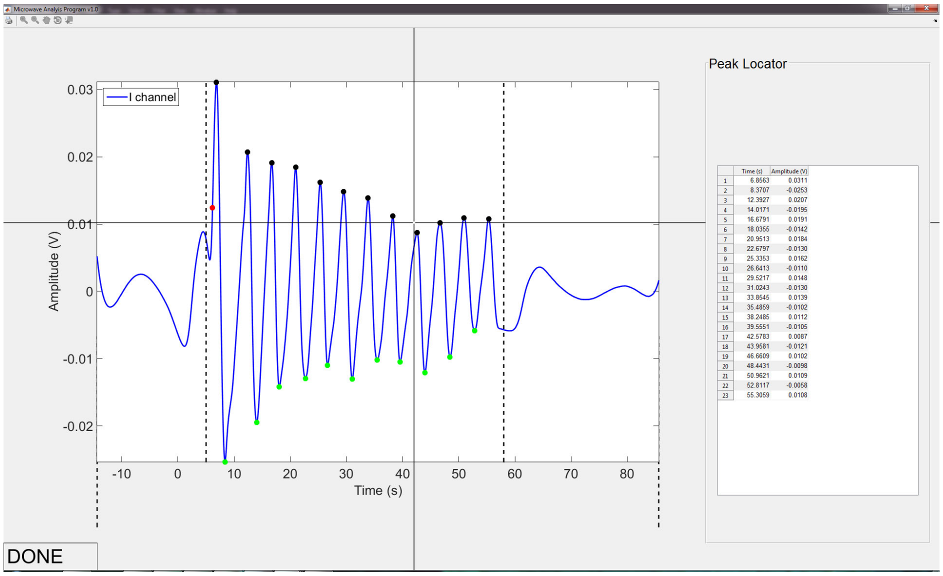

	Time (s)	Amplitude (V)
1	6.8563	0.0311
2	8.3707	-0.0253
3	12.3927	0.0207
4	14.0171	-0.0195
5	16.6791	0.0191
6	18.0355	-0.0142
7	20.9513	0.0184
8	22.6797	-0.0130
9	25.3353	0.0162
10	26.6413	-0.0110
11	29.5217	0.0148
12	31.0243	-0.0130
13	33.8545	0.0139
14	35.4859	-0.0102
15	38.2485	0.0112
16	39.5551	-0.0105
17	42.5783	0.0087
18	43.9581	-0.0121
19	46.6609	0.0102
20	48.4431	-0.0098
21	50.9621	0.0109
22	52.8117	-0.0058
23	55.3059	0.0108

Figure A.5: MWAP Peak Modifying screen.

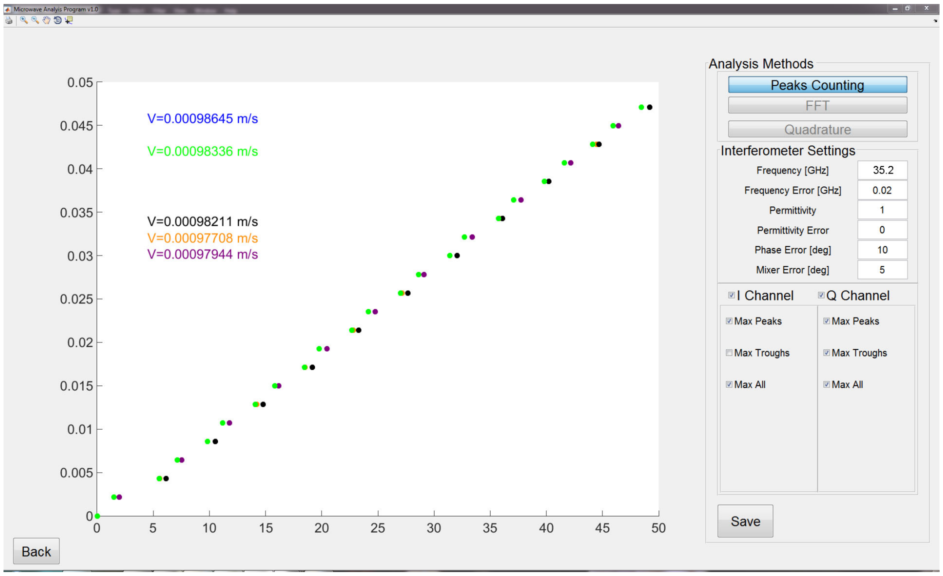

Interferometer Settings

Frequency [GHz] 35.2
Frequency Error [GHz] 0.02
Permittivity 1
Permittivity Error 0
Phase Error [deg] 10
Mixer Error [deg] 5

☑ I Channel
☑ Max Peaks
☐ Max Troughs
☑ Max All

☑ Q Channel
☑ Max Peaks
☑ Max Troughs
☑ Max All

Figure A.6: MWAP Peak Counting screen.

A.7, where the dashed black lines represent the error bounds. The slope, or velocity, is also displayed in the upper left corner. Images and text files of the quadrature results, along with the Lissajou, are saved using the **Save** button.

The FFT Analysis screen is shown in Figure A.8. Normalization of the signals is available to improve the frequency histogram. The velocity range (0 to that specified in **Max Velocity**) and the number of points in the FFT window are adjustable. The FFT histogram is visualized with the **Plot** button. Once again, the images and text files of the FFT histogram are saved using the **Save** button.

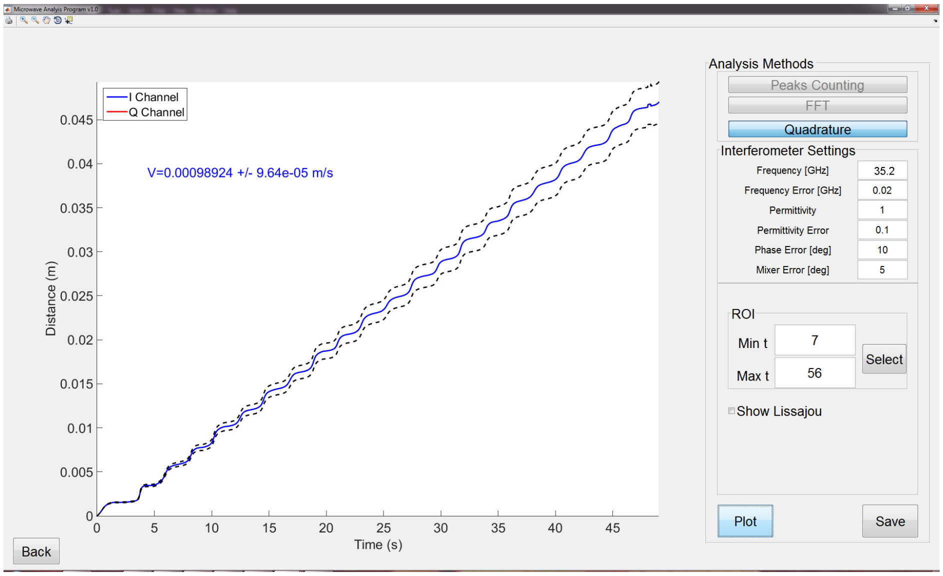

V=0.00098924 +/- 9.64e-05 m/s

Frequency [GHz] 35.2
Frequency Error [GHz] 0.02
Permittivity 1
Permittivity Error 0.1
Phase Error [deg] 10
Mixer Error [deg] 5
Min t 7
Max t 56
☐ Show Lissajou

Figure A.7: MWAP Quadrature Analysis screen.

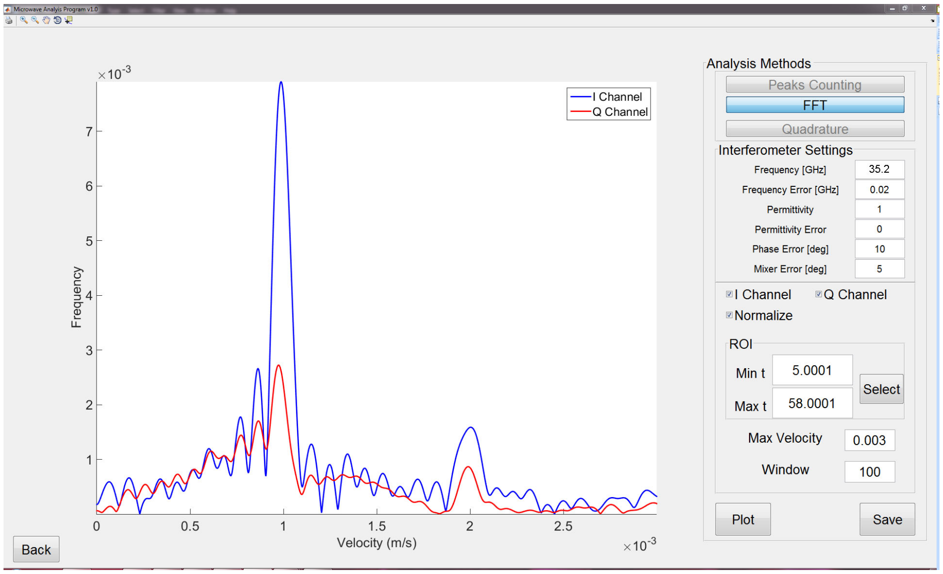

Frequency [GHz] 35.2
Frequency Error [GHz] 0.02
Permittivity 1
Permittivity Error 0
Phase Error [deg] 10
Mixer Error [deg] 5
☑ I Channel ☑ Q Channel
☑ Normalize
Min t 5.0001
Max t 58.0001
Max Velocity 0.003
Window 100

Figure A.8: MWAP FFT Analysis screen.

Appendix B

Single Laser MPMI Design

A schematic of the single laser design is presented in Figure B.1. The design follows closely to that of the two laser design. A single laser is sent through a commercial EO modulator. This imparts an amplitude modulation very close to the microwave frequency. The amplitude modulated laser is sent through the EO crystal and phase modulated by the reflected microwave signal. The polarization optics converts this phase lag into an amplitude modulation, giving two characteristic modulation frequencies to the laser. Once again, the system is designed such that the microwave frequency is measured and any Doppler shifts recorded.

A simplified mathematical treatment of the single laser interferometer is presented below. It is in a slightly different presentation than the two laser design for simplicity. The electric field of the laser is represented by the following.

$$E = A_0 \cos(\alpha) \tag{B.1}$$

A commercial EO modulator is used to modulate the laser's amplitude at a frequency $f_{EO} = \beta$, such that $|f_{EO} - f'_{MW}(t)| < f_d$. Once again, $f'_{MW}(t)$ represents the reflected microwave frequency and f_d represented the detector bandwidth. The EO modulated beam is represented with the following.

$$E = A_1 \left[C_1 + \cos(\beta)\right] \cos(\alpha) \tag{B.2}$$

Here, $C_1 \geq 1$ and is set along with A_1 to capture the field strength output by the EO modulator. The EO crystal imparts a modulation at the microwave frequency, $f'_{MW}(t) = \gamma$.

$$E = A_2[C_2 + \cos(\gamma)][C_1 \cos(\alpha) + \cos(\alpha)\cos(\beta)] \tag{B.3}$$

Once again, $C_2 \geq 1$ and is set along with A_2 to capture the field strength sent to the detector. The intensity recorded by the detector is represented with the following.

$$\begin{aligned} I =& A_2^2 C_1^2 C_2^2 \cos(\alpha)^2 + 2A_2^2 C_1^2 C_2 \cos(\alpha)^2 \cos(\gamma) + 2A_2^2 C_1 C_2^2 \cos(\alpha)^2 \cos(\beta) + \\ & 4A_2^2 C_1 C_2 \cos(\alpha)^2 \cos(\beta)\cos(\gamma) + A_2^2 C_1^2 \cos(\alpha)^2 \cos(\gamma)^2 + \\ & 2A_2^2 C_1 \cos(\alpha)^2 \cos(\beta)\cos(\gamma)^2 + A_2^2 C_2^2 \cos(\alpha)^2 \cos(\beta)^2 + \\ & 2A_2^2 C_2 \cos(\alpha)^2 \cos(\beta)^2 \cos(\gamma) + A_2^2 \cos(\alpha)^2 \cos(\beta)^2 \cos(\gamma)^2 \end{aligned} \tag{B.4}$$

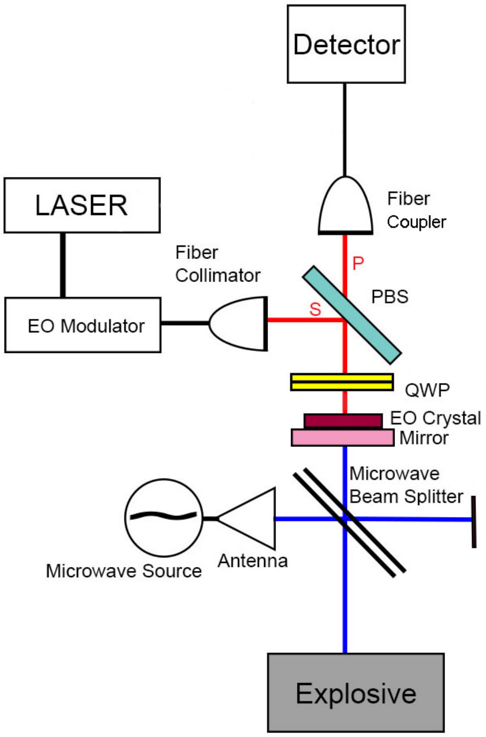

Figure B.1: Schematic illustrating the single laser MPMI concept.

Once again, the laser, microwave, and EO modulator frequencies are above f_d, leaving only the frequency difference between the microwave source and EO modulator detectable.

$$\langle I\rangle = \frac{1}{2}A_2^2C_1^2C_2^2 + \frac{1}{4}A_2^2C_1^2 + \frac{1}{4}A_2^2C_2^2 + \frac{1}{8}A_2^2 + A_3^2C_1C_2\cos(\beta-\gamma) \tag{B.5}$$

DISTRIBUTION:

1	MS 1189	John F. Benage Jr., Org. 1646
1	MS 1454	Leanna M.G. Minier, Org. 2554
1	MS 1454	Marcia A. Cooper, Org. 2554
1	MS 0386	Brook A. Jilek, Org. 2121
1	MS 1452	Joseph D. Olles, Org. 2554
1	MS 1189	Daniel H. Dolan, Org. 1646
1	MS 0359	D. Chavez, LDRD Office, 1911
1	MS 0899	Technical Library, 9536 (electronic copy)

Sandia National Laboratories